Julius-Maximilians-Universität Würzburg
Fakultät für Physik und Astronomie
Lehrstuhl für Astronomie

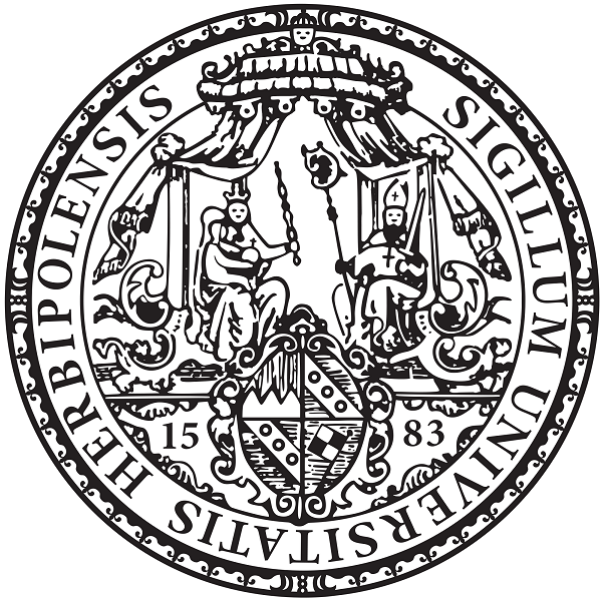

Bachelor Thesis

TANAMI VLBI Observations of PKS 0521−365

Author: Florian Rösch
Supervisor: Prof. Dr. Matthias Kadler
Date of Submission: April 21, 2016

Zusammenfassung

In dieser Arbeit werden neun TANAMI VLBI Epochen des Aktiven Galaxienkerns (AGN) PKS 0521−365, beobachtet bei einer Frequenz von 8.4 GHz, untersucht. AGN sind kompakte Regionen im Zentrum von Galaxien, deren elektromagnetische Strahlung die stellare Strahlung der gesamten zugehörigen Galaxie überstrahlt. Sie werden in verschiedene Gruppen klassifiziert, die in einem vereinheitlichten Modell zusammengefasst werden können. Einige AGN-Klassen emittieren Materiejets aus der Kernregion, deren Eigenschaften vor allem durch hochauflösende Beobachtungen untersucht werden können.

Very Long Baseline Interferometry (VLBI) ist eine der wichtigsten Methoden um die physikalischen Eigenschaften dieser Jets zu untersuchen. Dabei werden einzelne Radioteleskope zu Netzwerken zusammengefasst, was zu sehr großen Auflösungen führt. Mit dieser Methode können wichtige Eigenschaften der Jets, wie Geschwindigkeit β und Sichtwinkel ϕ, untersucht werden.

Das TANAMI (Tracking Active Galactic Nuclei with Austral Milliarcsecond Interferometry) Programm beobachtet extra-galaktische Jets südlich einer Deklination von $-30°$ und verbindet hochauflösende VLBI Beobachtungen bei Frequenzen von 8.4 GHz und 22.3 GHz mit Beobachtungen bei Frequenzen bei IR-, optischen/UV-, Röntgenstrahlungs- und γ-Strahlungsenergien.

PKS 0521−365 ist eine Quelle, deren Klassifizierung nicht klar ist. Zum einen kann sie als BL Lac Objekt klassifiziert werden, zum anderen als Radio Galaxie. Sie hat eine Rotverschiebung von $z = 0.056$ und zeigte zwischen Juni 2010 und Februar 2012 eine signifikante Aktivität im γ-Strahlenbereich.

In dieser Arbeit wurden Karten zu neun TANAMI Epochen von PKS 0521−365 erstellt. Die Bilder zeigen eine Jetstruktur mit einer Ausdehnung von ungefähr 80 pc. Das Verhältnis der Flussdichte von Jet zu Counter-Jet wurde zu $R > 95$ bestimmt. Außerdem wurde durch die Annahme eines möglichen Counterjets ein absolutes Minimum dieses Verhältnisses von $R > 4$ bestimmt.

Durch eine kinematische Analyse der TANAMI Daten, zusammen mit anderen VLBA und SHEVE Daten, konnte eine Obergrenze der scheinbaren Jetgeschwindigkeit von $\beta_{\mathrm{app}} < 0.36$ gefunden werden. Diese führt, zusammen mit $R > 95$, zu einer $\beta - \phi$ Ebene, die zu einer Untergrenze für die Jetgeschwindigkeit von $\beta \gtrsim 0.56$ und zu einer Obergrenze für den Sichtwinkel von $\phi \lesssim 16°$ führt, was vergleichbar mit früheren Ergebnissen von D'Ammando et al. (2015) ist, aber das Ergebnis von Pian et al. (1996) vollständig ausschließt. Auch für $R > 4$ liegt nur ein sehr kleiner Bereich dieses ausgeschlossenen Ergebnisses in der erlaubten $\beta - \phi$ Ebene. Deshalb legen die TANAMI VLBI Daten

einen kleineren Sichtwinkel als bisher vermutet nahe.

Die Flussdichte des Kerns ist bis zum März 2010 annähernd konstant und steigt dann signifikant an. Der Zeitraum, in dem dieser Anstieg geschieht, ist äquivalent zu dem Zeitraum, in dem die Quelle eine signifikante Aktivität im γ-Strahlenbereich zeigt. In diesem Zeitraum steigt auch die Helligkeitstemperatur des Kerns auf Werte, die oberhalb des sogenannten Compton-Limits liegen, was ebenfalls mit der Aktivität im γ-Strahlenbereich erklärt werden kann.

Abstract

In this thesis nine TANAMI VLBI epochs of the Active Galactic Nucleus (AGN) PKS 0521−365, observed at 8.4 GHz, were investigated. AGN are compact regions at the center of galaxies with an emission overwhelming the stellar emission of the entire galaxy. They are differentiated into several classes which can be united in the so called unification model. Some AGN emit extragalactic jets that can be investigated by high-resolution observations.

Very Long Baseline Interferometry (VLBI) is one of the main methods to investigate the physical properties of these jets. Therefor, an array of single radio telescopes is used leading to a very high resolution. So, important properties of extragalactic jets, such as the jet speed β or the viewing angle ϕ, can be investigated.

The TANAMI (Tracking Active Galactic Nuclei with Austral Milliarcsecond Interferometry) program observes extragalactic jets south of $-30°$ declination. It combines high-resolution VLBI observations at frequencies of 8.4 GHz and 22.3 GHz with higher-frequency observations at IR, optical/UV, X-ray and γ-ray energies.

PKS 0521−365 is an AGN with an unclear classification. Some classify it as a BL Lac object, while others classify it as a radio galaxy. PKS 0521−365 has a redshift of $z = 0.056$ and showed a significant γ-ray flaring activity between 2010 June and 2012 February.

In this thesis images of nine TANAMI epochs of PKS 0521−365 were produced and analyzed. These images show a knotty jet structure with an extension of around 80 pc. The jet to counterjet ratio of the flux density was estimated to be $R > 95$. Furthermore, an absolute minimum of that ratio was computed to be $R > 4$ using images with a possible counterjet.

The kinematic analysis of the TANAMI data, together with other VLBA and SHEVE data, leads to a limit of the apparent speed of $\beta_{\mathrm{app}} < 0.36$. Using $R > 95$, an allowed $\beta - \phi$ plane was computed leading to a lower limit of the jet speed of $\beta \gtrsim 0.56$ and an upper limit of the viewing angle of $\phi \lesssim 16°$ corresponding to the result of D'Ammando et al. (2015). But, this $\beta - \phi$ plane completely rules out the result of Pian et al. (1996). Even, if $R > 4$ is used to constrain the $\beta - \phi$ plane, only a marginal fraction of that result is located in the allowed $\beta - \phi$ plane. Therefore, the TANAMI VLBI data suggest a smaller inclination angle of the jet than previously thought.

The flux density of the core component is nearly constant until 2010 March. Thereafter, it increases significantly corresponding to the γ-ray flaring activity between 2010 June and 2012 February. In this period also the brightness temperature of the core component lies above the inverse Compton limit, which can also be explained by the

γ-ray flaring activity.

Contents

1. Scientific Context

1.1. Active Galactic Nuclei (AGN)

Active galactic nuclei (AGN) are compact regions at the center of galaxies with a supermassive black hole (SMBH) as central engine causing an emission overwhelming the stellar emission of the entire galaxy. The strong gravitational potential of the SMBH pulls the surrounding materials inwards, forming an accretion disc of hot plasma. Roughly perpendicular to this disc, there is the additional presence of relativistic jets in radio-loud objects (Kembhavi and Narlikar 1999).

The continuum radiation from AGN stretches over the entire range of the electromagnetic spectrum, from the radio to the high-energy γ-ray region. The continuum spectrum has an overall complex shape, but can often be approximated by a simple power law form over fairly wide wavelength intervals, i.e. $S(\nu) \propto \nu^{\alpha}$, where $S(\nu)$ is the flux density at a specific frequency ν and α is the spectral index. The radiation is emitted through elementary processes such as synchrotron emission, bremsstrahlung and inverse Compton scattering, and modified by scattering, absorption and reemission (Kembhavi and Narlikar 1999).

The following Sections will give a brief overview of the physical properties of AGN. If no additional references are given, this Chapter is based on the textbook by Kembhavi and Narlikar (1999).

1.1.1. Classification and Unification

One first step towards classifying AGN, is to differentiate them into radio-loud and radio-quiet sources. According to Kellermann et al. (1989) the ratio $R_{\mathrm{r-o}}$ of the radio flux density S_{r} to the optical flux density S_{o} can be used:

$$R_{\mathrm{r-o}} = \frac{S_{\mathrm{r}}}{S_{\mathrm{o}}}. \tag{1.1.1}$$

For radio-quiet AGN the ratio is $0.1 < R_{\mathrm{r-o}} < 1$, while for radio-loud sources the ratio obtains $R_{\mathrm{r-o}} > 10$.

The next step is to distinguish AGN by their emission spectrum, which leads to the so called AGN-Zoo. Therefore, radio-quiet sources can be differentiated into Seyfert galaxies and radio-quiet quasars, while radio-loud sources can be divided into radio-loud quasars, blazars and radio galaxies.

Seyfert Galaxies

Seyfert (1943) found a class of galaxies with bright star-like nuclei and strong broad emission lines. These so called Seyfert galaxies are radio-quiet and appear to have the morphology of spiral galaxies. Following the textbook of Kembhavi and Narlikar (1999) Seyfert galaxies can be distinguished on the basis of their emission line properties into Seyfert type 1 and Seyfert type 2 galaxies. A Seyfert 1 galaxy has a bright star-like nucleus that emits strong continuum emission from the far infrared to the X-ray band. It has broad allowed emission lines and narrow forbidden lines. A Seyfert 2 galaxy has a weak continuum and only strong narrow forbidden lines. In contrast to a Seyfert 1 galaxy, it does not have broad lines.

Quasars

Quasar is the acronym for *quasi-stellar radio source*. Historically quasars were star-like objects identified with strong radio sources, while objects which had the optical properties of quasars but which did not necesserily have strong radio emission, were called *quasi-stellar objects* (QSO). The optical spectrum of QSOs is very similar to those of Seyfert galaxies, but they have a higher luminosity. Today the distinction between quasar and QSO is not very much in use. According to Kellermann et al. (1989) there are about 10 times more radio-quiet QSOs than radio-loud ones.

Blazars

Blazars are compact radio sources that have strong continua, with a flat or inverted spectrum. They can be divided into sub-classes. Objects with strong emission lines are called *flat spectrum radio quasars* (FSRQ), while objects with absent or weak emission lines are called BL Lacertae (BL Lac) objects. BL Lac objects have strong nuclear continuum radiation that shows high polarization and rapid variability. Emission lines are, however, absent or weak. All known examples are strong radio sources and they are sometimes found to be the nuclei of elliptical galaxies. Furthermore, BL Lac objects are less luminous than FSRQs.

Radio Galaxies

Radio galaxies are associated with elliptical galaxies with bright optical nuclei emitting strong continuum radiation. In optical wavelength they can be divided in two sub-classes similar to the Seyfert galaxies. *Broad line radio galaxies* (BLRG) have emission lines resembling those from Seyfert 1 galaxies, while *narrow line radio galaxies* (NLRG) have spectra like the Seyfert 2 galaxies. So NLRG and BLRG can be seen as radio-loud counterparts of Seyfert galaxies. Independent of the optical-spectral classification scheme, the radio morphology can be distinguished into so called Fanaroff-Riley classes. According to Fanaroff and Riley (1974) *Fanaroff-Riley type 1* (FR 1) galaxies have bright,

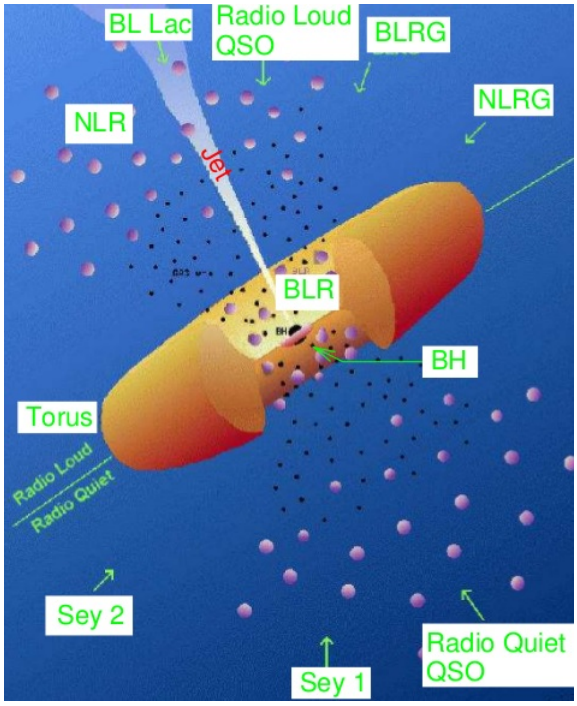

Figure 1.1.: Unification model after Urry and Padovani (1995). The lower part shows the model for radio-quiet AGN while the upper part represents the model for radio-loud AGN. BH stands for the black hole, BLR and NLR for *broad line region* and *narrow line region*, BLRG and NLRG for *broad line radio galaxy* and *narrow line radio galaxy*, Sey 1 and Sey 2 for Seyfert 1 and Seyfert 2 galaxies.

dominant nuclei and two asymmetric broad jets ending in plumes. *Fanaroff-Riley type 2* (FR 2) galaxies, which are more luminous than FR 1 galaxies, often have only one-sided weak jets ending in radio lobes. In contrast to FR 1 galaxies these lobes dominate the radio spectra of FR 2 galaxies.

Unification Model

All AGN classes mentioned above can be united in a unification model. According to Urry and Padovani (1995) and Antonucci (1993) all AGN types are caused by the same physics and the different phenomenology can be explained with different viewing angels between the jet axis and the line of sight. Figure 1.1 illustrates the concept of this model.

The subsequent explanations follow Antonucci (1993). The central engine of all AGN is a super-massive black hole (SMBH), surrounded by an accretion disc at a distance of about $r \approx 10^{-3}\,\mathrm{pc}$ and a density of about $n \approx 10^{15}\,\mathrm{cm}^{-3}$. Around the accretion disc, at a distance of about $r \approx 0.01\,\mathrm{pc}$ up to $r \approx 0.1\,\mathrm{pc}$ from the SMBH, there is the so called *broad line region* (BLR) with a density of about $n \approx 10^{10}\,\mathrm{cm}^{-3}$. At a distance of

about $r \approx 1\,\mathrm{pc}$ up to a few $10\,\mathrm{pc}$, a cold dust torus is located with densities between $n \approx 10^3$ and $n \approx 10^6\,\mathrm{cm}^{-3}$. Finally, the *narrow line region* (NLR) can be found at distances between $r \approx 100$ and $r \approx 1000\,\mathrm{pc}$ with the same density range as the torus. In radio-loud AGN there is also the presence of relativistic jets perpendicular to the accretion disc. These jets are conduits for the transport of energetic particles from the nucleus to the extended radio structures (Kembhavi and Narlikar 1999).

With the help of this model, the characteristics of the different AGN types can be explained using three distinctive parameters, namely the radio loudness, the viewing angle between the jet axis and the line of sight, and the luminosity.

As one can see at the radio-quiet side of Fig. 1.1, Seyfert 2 galaxies have large viewing angles, so the torus obscures the BLR and only narrow emission lines from the NLR are visible. The viewing angle of Seyfert 1 galaxies is smaller, compared to that of Seyfert 2 galaxies, so the BLR can also be seen. That explains the fact that Seyfert 1 galaxies have broad and narrow emission lines, while Seyfert 2 galaxies have only narrow lines.

At the radio-loud side of Fig. 1.1, the torus also hides the BLR for NLRG, because of their large viewing angle. So, only narrow emission lines can be seen. Because of the smaller viewing angles of BLRG, also broad emission lines can be detected. The absent emission lines of BL Lac objects can be explained with the very small viewing angle, so the radio jet directly points to the observer and outshines the emission lines from the NLR and the BLR. This small angle also leads to apparent superluminal motion and Doppler boosting of the observed flux density (see Sect. 1.1.4).

With the third additional parameter, namely the luminosity, a further differentiation of the AGN classes is possible. For example, as mentioned above, radio-quiet QSOs and Seyfert galaxies have similar optical spectra, but they can be distinguished by their luminosities, because Seyfert galaxies are less luminous than radio-quiet QSOs.

1.1.2. Emission Processes

AGN emit radiation throughout the entire electromagnetic spectrum. While synchrotron losses dominate the low frequency emission, the origin of the high-energy emission is still unclear, with leptonic and hadronic emission models being discussed. Here, these emission processes will be explained briefly following the descriptions of Rybicki and Lightman (1979) for the leptonic emission models.

Synchrotron Radiation

Synchrotron radiation is emitted when a relativistic charged particle is accelerated by a magnetic field. The motion of a charged particle in a magnetic field $\vec{B}$ is described in classical electrodynamics by the Lorentz force equation

$$\frac{d}{dt}(\gamma m \vec{v}) = \frac{e}{c}(\vec{v} \times \vec{B}), \tag{1.1.2}$$

where e and m are the charge and rest mass of the particle, $\vec{v}$ is the velocity and $\gamma = (\sqrt{1-\beta^2})^{-1}$ the Lorentz factor, with $\beta = \frac{v}{c}$, where c is the speed of light. According to Equation (1.1.2), the acceleration of the particle is normal to the velocity and the magnetic field, so v and γ are constant and there is no force in the direction of the magnetic field. Therefore, the particle moves in a helix with its axis parallel to $\vec{B}$ with the gyration frequency $\nu_\mathrm{g} = \frac{eB}{2\pi\gamma mc}$. This leads to the emitted power of

$$P = \frac{2}{3} r_0^2 c \beta^2 \gamma^2 B^2 \sin^2 \alpha, \tag{1.1.3}$$

where α is the angle between the velocity and the magnetic field, called pitch angle, and $r_0 = \frac{e^2}{mc^2}$. Because these emitted power is proportional to m^{-2}, synchrotron radiation from an electrically neutral plasma is overwhelming from the electrons.

An important effect of the relativistic motion is that the radiation is concentrated in a narrow cone with axis in the direction of $\vec{v}$ and half-angle $\propto \gamma^{-1}$. As the electron moves in a helix around the magnetic field, an observer whose line of sight happens to intersect the cone sees a sequence of pulses with a period equal to the Doppler shifted gyration frequency ν'_g. The frequency spectrum of this radiation consists of a series of points at ν'_g and its harmonics. If radiation from an ensemble of particles is considered, this spectrum appears to be continuous with a maximum at the critical frequency $\nu_\mathrm{c} \propto E^2$, where E is the energy of the electrons. Then, the emitted power is given by

$$P(E,\nu) = \frac{\sqrt{3} e^2 B \sin\alpha}{mc^2} F\left(\frac{\nu}{\nu_\mathrm{c}}\right), \tag{1.1.4}$$

with the function $F(x) = x \int_x^\infty K_{5/3}(\xi) d\xi$, where $K_{5/3}(\xi)$ is the modified Bessel function of order $\frac{5}{3}$. If the number density of an ensemble of electrons with energy between E and $E + dE$ is given by $n(E)dE$, the emitted power is given by

$$P(\nu) = \int_{E_1}^{E_2} P(E,\nu) n(E) dE. \tag{1.1.5}$$

For nonthermal synchrotron radiation the number density of the electrons follows a power law: $n(E)dE = CE^{-p}dE$, where C is constant. Therefore, the emitted spectrum is of the simple power law form

$$P(\nu) \propto \nu^{-\alpha}, \tag{1.1.6}$$

where $\alpha = \frac{p-1}{2}$ is the spectral index.

These simple power law form can only be observed for an optically thin medium. The optical depth τ_ν is defined by $\tau_\nu = \alpha_\nu l$, where α_ν is the absorption coefficient and l is the length of the medium. A medium is called optically thin for $\tau_\nu < 1$ and optically thick for $\tau_\nu > 1$. In an optically thick medium electrons absorb the low-energy photons that were emitted previously as synchrotron radiation. This process is called synchrotron self-

absorption and leads to a flux density $S(\nu) \propto \nu^{5/2}$, which means, that the spectral index $\alpha = \frac{5}{2}$ is constant and independent of p. Since the absorption coefficient is inversely dependent on the frequency, this process occurs only below a critical frequency, where $\tau_\nu = 1$. At all higher frequencies the medium is optically thin and the flux density is given by $S(\nu) \propto \nu^{-\frac{p-1}{2}}$.

Inverse Compton Scattering

Inverse Compton scattering causes the high-energy emission in leptonic models.

Compton scattering is the inelastic scattering of photons by electrons. This leads to an energy-gain for the electron, while the energy of the photon decreases. Depending upon the kinematics of the collision, energy can pass also from the electron to the photon, if the electron is already in motion. Therefore, the photon gains energy and the electron loses energy. This process is called inverse Compton scattering. If the needed photons for this process are synchrotron photons emitted by energetic electrons from the same set of electrons that is responsible for the synchrotron emission, this process is called Synchrotron Self-Compton (SSC).

The energy-loss of the electrons due to inverse Compton scattering can cool down the complete electron gas, which can lead to the so called Compton catastrophe. These inverse Compton cooling leads to the Compton limit of the brightness temperature of $T_\mathrm{B} \sim 10^{12}\,\mathrm{K}$ (see also Sect. 1.1.3).

Hadronic Emission Models

In hadronic models, the low frequency emission is also dominated by electron-synchrotron emission, but the high-energy emission is produced via hadronic particles. A part of the jet power can be used to accelerate relativistic protons, which leads to pion production by photon-proton interactions. These pions decay in an electromagnetic particle cascade producing high-energy photons (Mannheim and Biermann 1992; Mannheim 1993). According to Böttcher (2010) magnetic fields of several tens of Gauss are needed to accelerate protons to such high energies. In such high magnetic fields also proton-synchrotron radiation must be taken into account.

1.1.3. Brightness Temperature

The brightness temperature is, according to Burke and Graham-Smith (2010), that temperature of an emitter of radiation at frequency ν that it would need to have if it were a black body. If modeling relativistic jets with Gaussian components (see Sect. 1.2.3), the brightness temperature of such a component can be calculated following Kovalev et al. (2005) to be

$$T_\mathrm{B} = \frac{2\ln 2}{\pi k_\mathrm{B}} \frac{S\lambda^2(1+z)}{a_\mathrm{maj} a_\mathrm{min}}, \tag{1.1.7}$$

where S is the flux density of the component, a_{maj} and a_{min} are the FWHMs of the elliptical Gaussian components along the major and minor axes, λ is the wavelength of observation, z is the redshift of the source and k_{B} is the Boltzmann constant.

There are two limits to the maximum brightness temperature. The above mentioned inverse Compton limit of $10^{12}\,\mathrm{K}$ and the equipartition value of $10^{11}\,\mathrm{K}$ (Kovalev et al. 2005). According to Kellermann and Pauliny-Toth (1969) these limits can be calculated by the ratio of the intensity of the radiation from inverse Compton scattering L_{C} relative to the synchrotron emission L_{S}, which is equal to the ratio of the energy density in the radiation field u_{rad} to that in the magnetic field u_{B}. This ratio can be written in terms of the maximum brightness temperature T_{max}

$$\frac{L_{\mathrm{C}}}{L_{\mathrm{S}}} = \frac{u_{\mathrm{rad}}}{u_{\mathrm{B}}} \sim \frac{1}{2}\left(\frac{T_{\mathrm{max}}}{10^{12}}\right)^5 \nu_{\mathrm{c}} \left[1 + \frac{1}{2}\left(\frac{T_{\mathrm{max}}}{10^{12}}\right)^5 \nu_{\mathrm{c}}\right], \tag{1.1.8}$$

where ν_{c} is the upper cutoff frequency of the radio spectrum in MHz, probably $\nu_{\mathrm{c}} \sim 10^{5\pm1}$, and the second term represents the effect of second-order scattering. So, for $T_{\mathrm{max}} < 10^{11}\,\mathrm{K}$, $\frac{L_{\mathrm{C}}}{L_{\mathrm{S}}} < 1$, but for $T_{\mathrm{max}} > 10^{12}\,\mathrm{K}$ second-order scattering is important and the energy losses due to inverse Compton scattering become catastrophic. Then, the brightness temperature decreases to $10^{11}\,\mathrm{K} \lesssim T_{\mathrm{B}} \lesssim 10^{12}\,\mathrm{K}$, where inverse Compton losses are of the same order as the synchrotron losses. So, the ratio of Equation (1.1.8) becomes one, which is called equipartition.

According to Readhead (1994) equipartition is a state that holds for many years, whereas for $T_{\mathrm{B}} \sim 10^{12}\,\mathrm{K}$, inverse Compton scattering dominates and an emission region will radiate away most of its energy in a timescale of days, which motivates the term "catastrophe". Nevertheless, many sources have brightness temperatures beyond the equipartition value or the inverse Compton limit, which can be explained by Doppler boosting, transient nonequilibrium events, coherent emission, emission by relativistic protons or a combination of these effects (Kovalev et al. 2005).

1.1.4. Jet Kinematics and Morphology

One of the early observational results of VLBI (see Sect. 1.2) was that some compact radio sources consist of more than one component, which move with apparent speeds higher than the speed of light. This seems to be unphysical, but can be explained by a projection effect.

Consider a single component moving towards an observer with speed v and angle ϕ to the line of sight, emitting signals at t_0 and $t_1 = t_0 + \Delta t_{\mathrm{emit}}$ (see Fig. 3.5). During the time Δt_{emit} the component moves a distance $v\Delta t_{\mathrm{emit}} \cos\phi$ in the direction of the observer. Due to the reduction in the distance, the signals arrive in a time interval

$$\Delta t_{\mathrm{obs}} = \left(1 - \frac{v}{c}\cos\phi\right)\Delta t_{\mathrm{emit}}. \tag{1.1.9}$$

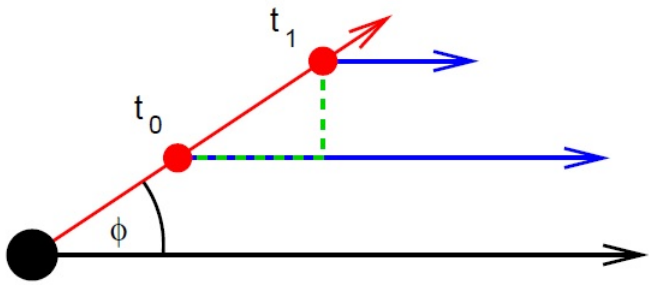

Figure 1.2.: This sketch illustrates a single component moving towards an observer with speed v and angle ϕ with respect to the line of sight. The component emits signals at t_0 and t_1. Taken from Kadler (2015).

Otherwise, the observed distance the component travels in the plane of sky is given by $\Delta l = v\Delta t_{\rm emit} \sin\phi$. Therefore, the apparent speed $v_{\rm app}$ is given by

$$v_{\rm app} = \frac{\Delta l}{\Delta t_{\rm obs}} = \frac{v \sin\phi}{1 - \frac{v}{c}\cos\phi}, \tag{1.1.10}$$

which leads to $v_{\rm app} > c$ for large $\beta = \frac{v}{c}$ and small ϕ. With $\beta_{\rm app} = \frac{v_{\rm app}}{c}$, Equation (1.1.10) can be rewritten into

$$\beta_{\rm app} = \frac{\beta \sin\phi}{1 - \beta\cos\phi}. \tag{1.1.11}$$

Another relativistic effect is the so called Doppler boosting. If a source moves at relativistic speed towards an observer, the observed flux density is Doppler boosted to higher levels, while the flux density of a source moving away from the observer can be greatly reduced. Therefore, a two-sided radio jet can appear to be one-sided.

To obtain an expression for the Doppler boosting of the flux density one needs to perform a Lorentz transformation between the observed frequency $\nu_{\rm obs}$ and the emitted frequency $\nu_{\rm emit}$. The Doppler factor δ then is defined by

$$\delta = \frac{\nu_{\rm obs}}{\nu_{\rm emit}} = \frac{1}{\gamma(1 - \beta\cos\phi)} = \frac{\sqrt{1-\beta^2}}{1 - \beta\cos\phi}. \tag{1.1.12}$$

If $I(\nu)$ is the intensity of radiation, it can be shown that $I(\nu)\nu^{-3}$ is a Lorentz invariant. Because the flux density $S(\nu) \propto I(\nu)$, for a source with power law spectrum $S(\nu) \propto \nu^{-\alpha}$ follows

$$S_{\rm obs}(\nu_{\rm obs}) = \delta^{3+\alpha} S_{\rm emit}(\nu_{\rm obs}), \tag{1.1.13}$$

where $S_{\rm emit}$ is the emitted flux density and $S_{\rm obs}$ is the observed flux density. Now consider a two-sided jet, where a jet component moves towards the observer and a counterjet component, with identical emitted flux density, moves away from the observer with the

same speeds v and with line-of-sight angles ϕ and $\pi + \phi$ respectively. Then, using the Equations (1.1.12) and (1.1.13), the ratio of the observed flux densities is given by

$$R = \frac{S_{\text{jet}}}{S_{\text{counter}}} = \left(\frac{1 + \beta \cos \phi}{1 - \beta \cos \phi} \right)^{p}, \tag{1.1.14}$$

where $p = 3 + \alpha$, if one observes several components, and $p = 2 + \alpha$, if one observes a continuous jet that can be expressed as a series of components.

1.2. Very Long Baseline Interferometry (VLBI)

Very Long Baseline Interferometry (VLBI) observations play a particular role in investigating the physics of AGN (Kellermann and Moran 2001). According to Carroll and Ostlie (2014) the angular resolution Θ of a single radio telescope is given by

$$\Theta = 1.22\frac{\lambda}{D}, \tag{1.2.1}$$

where λ is the wavelength and D is the diameter of the telescope. The intensity distribution of an incoming signal can be calculated by a Bessel's function, so the approximation of the first Bessel's function becoming zero leads to the numerical factor 1.22.

To improve the angular resolution for an observation at a given wavelength, the diameter of the telescope has to be increased. This can be done by synchronization of multiple radio telescopes called radio interferometry. Then, the diameter is given by the largest baseline, which is the connection of the reflection centers of two telescopes. To reach the best angular resolution very long baselines of thousands of kilometers are realized in VLBI arrays. The following explanations and descriptions of this Section follow the textbook by Burke and Graham-Smith (2010).

1.2.1. Radio Interferometry

Because the simplest array of telescopes consists of two identical antennas, the concept of radio interferometry will be explained by the so called two element interferometer shown in Fig. 1.3.

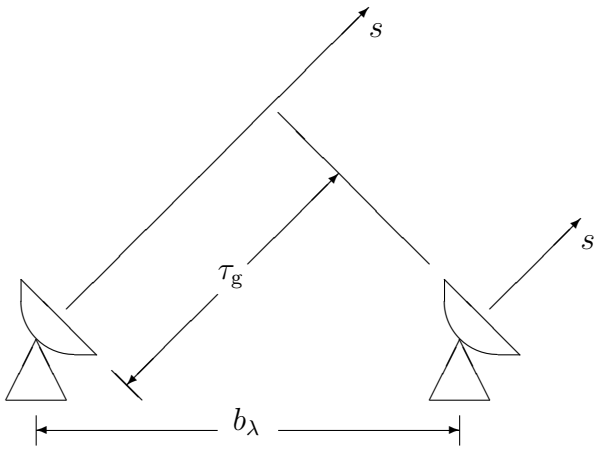

Figure 1.3.: Two element interferometer, after Burke and Graham-Smith (2010), consisting of two identical radio telescopes.

The power received by one single telescope is given by

$$P = \int_0^\infty d\nu A_{\text{eff}}(\nu) S(\nu), \tag{1.2.2}$$

where $S(\nu)$ is the flux density of the source, given by its brightness distribution integrated over the solid angle, and $A_{\text{eff}}(\nu)$ is the effective area of the dish. If two of these telescopes, connected by the baseline vector $\vec{b}$, point at a radio source under the direction given by the unit vector $\vec{s}$, the signal arrives at the second antenna delayed by the geometrical time delay $\tau_{\text{g}} = \frac{\vec{b}\cdot\vec{s}}{c}$. The first antenna is designated the reference antenna. The two signals are fed to a voltage multiplier. To correlate the data, an additional instrumental time delay τ_{i} can be inserted to equalize the signal delays, but in any case, the cross-correlation function $R(\tau)$ must be computed. It is given by the time-averaged product of two amplitudes (voltages), $x(t)$ and $y(t)$, with one delayed by time τ: $R_{\text{xy}}(\tau) = \langle x(t)y(t-\tau)\rangle$. For a monochromatic source these amplitudes will be $x(t) = v_1 \cos(2\pi\nu t)$ and $y(t) = v_2 \cos[2\pi\nu(t-\tau_{\text{g}})]$. Because the cross-correlation is equal to the power received from the source, according to Equation (1.2.2) it must be proportional to the effective antenna area $A_{\text{eff}}(\vec{s})$ and the source flux density S:

$$R_{\text{xy}}(\tau_{\text{g}}) = A_{\text{eff}}(\vec{s}) S \cos(2\pi\nu\tau_{\text{g}}) = A_{\text{eff}}(\vec{s}) S \cos(2\pi\vec{b}_\lambda\vec{s}), \tag{1.2.3}$$

where $\vec{b}_\lambda = \frac{\vec{b}}{\lambda}$ is the baseline vector measured in wavelengths.

Up to this point, τ_{i} has been set to zero, but now a source is considered whose position is close to a reference position $\vec{s}_0$ defined by the condition $\tau_{\text{g}} = \tau_{\text{i}}$. This position is called the phase-tracking center. Then, the direction to the source, with respect to the phase-tracking center, can be written $\vec{s} = \vec{s}_0 + \vec{\sigma}$, where $\vec{\sigma}$ is a small vector normal to $\vec{s}_0$. Since the large geometrical delay associated with $\vec{s}_0$ is exactly compensated for by the instrumental time delay, only the small differential associated with $\vec{\sigma}$ affects the time delay in the following analysis.

For an array of many telescopes, a given interferometer pair using the ith and jth elements of the array will have a baseline vector $\vec{b}_{\text{ij},\lambda}$. Furthermore, the instrumental delay is usually set so that it cancels out the tracking-center delay and in this limit the complex visibility V_{ij} can be defined by

$$V_{\text{ij}} = \int_{4\pi} A_{\text{eff}}(\vec{\sigma}) B_\nu(\vec{\sigma}) e^{i2\pi\vec{b}_{\text{ij},\lambda}\cdot\vec{\sigma}} d\Omega, \tag{1.2.4}$$

where B_ν is the brightness distribution of the observed source and $d\Omega$ is the solid angle of the source. The amplitude and phase of the complex visibility are the principal observables in interferometry and are connected to the brightness distribution on the sky $B_\nu(\vec{\sigma})$ via Fourier transformation.

Now let the coordinates of the baseline vector be given in a right-handed rectilinear

coordinate system (u, v, w), where $\vec{s}_0$ is parallel to the w-direction and perpendicular to the (u, v)-plane, meaning that $w = 0$. Therefore, the offset vector $\vec{\sigma}$ is parallel to the (u, v)-plane. Because all coordinate distances will be expressed in wavelengths, Equation (1.2.4) becomes

$$V_{\mathrm{ij}}(u, v) = \int_{4\pi} A_{\mathrm{eff}}(l, m) B_\nu(l, m) e^{i2\pi(ul+vm)} d\Omega, \tag{1.2.5}$$

where the coordinates (l, m, n) are the direction cosines of the unit vector $\vec{s}$. Thus, the coordinates of $\vec{\sigma}$ are (l, m) and the solid angle can be written $d\Omega = \frac{dldm}{\sqrt{1-l^2-m^2}}$. By small-angle approximation that is most familiar to the observer, Equation (1.2.5) becomes

$$V_{\mathrm{ij}}(u, v) = \int\int A_{\mathrm{eff}}(x, y) B_\nu(x, y) e^{i2\pi(ux+vy)} dxdy, \tag{1.2.6}$$

where the celestial angular coordinates (x, y) are the small-angle approximation of the coordinates (l, m).

Equation (1.2.6) shows that the visibility in the (u, v)-plane is the Fourier transformed of the brightness distribution in the (x, y)-plane. The problem of radio interferometry is that it is impossible to cover the entire (u, v)-plane. Thus, there is a loss of Fourier components in the synthesized image. So, the rotation of the earth is used to cover the empty spaces in the (u, v)-plane, which is called Earth rotation synthesis. Figure 1.4 shows the (u, v)-plane coverage of the Australia Telescope Compact Array (ATCA) in the 6A configuration, while using six telescopes at an observation time of 12 hours at different declinations. By this method the baseline between two fixed telescopes fills an elliptical closed trajectory in the (u, v)-plane within 12 hours. For a declination of $\pm 90°$ the ellipse becomes a circle, while for a declination of $0°$ it becomes a line.

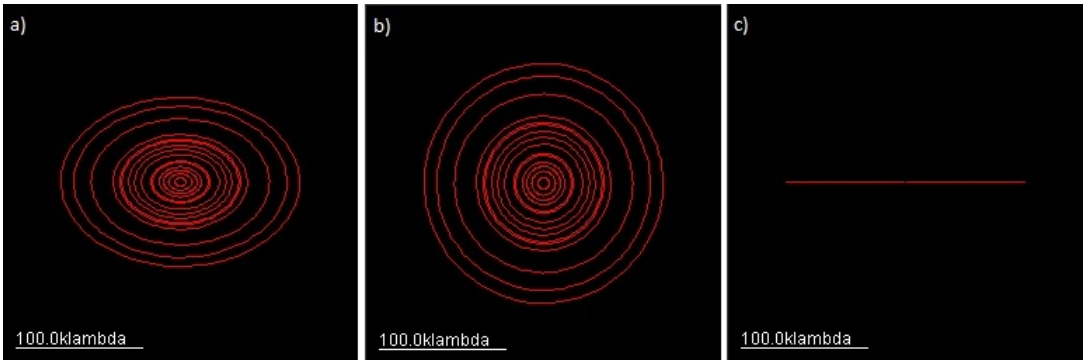

Figure 1.4.: The (u, v)-plane coverage of the ATCA array in the 6A configuration using six telescopes for a twelve-hour tracking observation at: a) $-45°$ declination, b) $-90°$ declination and c) $0°$ declination. The plots were made with the Virtual Radio Interferometer (VRI)[1].

[1] http://www.narrabri.atnf.csiro.au/astronomy/vri.html, 17.03.2016

1.2.2. TANAMI

The Tracking Active Galactic Nuclei with Austral Milliarcsecond Interferometry (TANAMI) program is a parsec-scale multiwavelength monitoring program that observes extragalactic jets south of −30 degrees declination. The information of this Section is taken from the papers of Kadler et al. (2015) and Ojha et al. (2010).

TANAMI, that originally started as a radio program with its focus on high-resolution VLBI observations, combines high-resolution imaging and spectral monitoring at radio wavelengths with higher-frequency observations at IR, optical/UV, X-ray and γ-ray energies. There is also a close cooperation with ANTARES, which is an undersea neutrino telescope that achieves its highest sensitivity at declinations south of about $-30°$, identical with the TANAMI sky. At these declinations TANAMI is the only large VLBI monitoring program. Other than most large VLBI programs, TANAMI observes at two frequencies, namely 8.4 GHz and 22.3 GHz. Therefore, the spectral indices for the core as well as bright jet components can be measured.

TANAMI uses a southern hemisphere VLBI network consisting of the five telescopes of the Australian Long Baseline Array (LBA), an antenna at Hartebeesthoek, South Africa, and the 34 m and 70 m telescopes of the NASA Deep Space Network in Tidbinbilla, near Canberra in the Australian Capital Territory (ACT). Additionally, observations

Table 1.1.: Telescopes of the TANAMI array, according to Müller (2014).

Telescope	Diameter [meters]	Location
Parkes	64	Parkes, New South Wales, Australia
ATCA	5×22	Narrabri, New South Wales, Australia
Mopra	22	Coonabarabran, New South Wales, Australia
Hobart	26	Mt. Pleasant, Tasmania, Australia
Ceduna	30	Ceduna, South Australia, Australia
Hartebeesthoek[a]	26	Hartebeesthoek, South Africa
DSS 43[b]	70	Tidbinbilla, ACT, Australia
DSS 45[b]	34	Tidbinbilla, ACT, Australia
O'Higgins[c]	9	O'Higgins, Antarctica
TIGO[c]	6	Concepcion, Chile
Warkworth	12	Aukland, New Zealand
Katherine	12	Northern Territory, Australia
Yarragadee	12	Western Australia
ASKAP	36×12	Murchinson, Western Australia

Note: (a) Unavailable between Sept. 2008 and Sept. 2010.
(b) Operated by the Deep Space Network of the National Aeronautics and Space Administration.
(c) Operated by the German Bundesamt für Kartographie und Geodäsie (BKG).

are made with the two German antennas, GARS at O'Higgins, Antarctica, and TIGO at Concepcion, Chile. Also, antennas in Yarragadee, Western Australia, Katherine, Northern Territory, Warkworth, New Zealand, and a single ASKAP antenna, also in Western Australia, are part of TANAMI observations. Details of all of these telescopes used in TANAMI observations are summarized in Table 1.1.

1.2.3. Analysis of VLBI Data

The first step analyzing VLBI data is an initial amplitude and phase calibration using the National Radio Astronomy Observatory's Astronomical Image Processing System (`AIPS`) software (Greisen 2003). Because this was not part of this thesis, no more information about `AIPS` will be given here. Nevertheless, more information about `AIPS` can be found in Cotton (1995) and Diamond (1995).

To produce an image of the VLBI data, first the visibility function must be Fourier transformed and then the beam pattern and the brightness distribution must be deconvolved. This can be done by the `clean` algorithm (Högbom 1974) included in the program `DIFMAP` (Shepherd 1997). The following descriptions of this program follows the `DIFMAP`-cookbook by Taylor (1997) and the user manual of `DIFMAP`.

First of all, one must choose the weighting of the data. If natural weighting is chosen, all data points are weighted equally, while with uniform weighting the data are weighted inversely to the number of visibilities. Natural weighting provides higher sensitivity than uniform weighting, but uniform weighting provides higher resolution.

After that, the imaging process can be started by opening a so called dirty map, where windows must be set around the brightest regions of this map. In this windows the `clean` algorithm models the brightness distribution of the source by setting a point source starting model and subtracting the flux density given by this model from the flux density given by the data. Thus, `clean` takes the residual dirty map and iteratively subtracts the dirty beam pattern convolved with the loop-gain times the brightest residual pixel. The final result is a new residual dirty map and a set of δ-components representing the flux density subtracted from the selected pixels in the defined windows.

The cleaning process is combined with self-calibration in amplitude and phase. According to Felli and Spencer (1989) for an only phase self-calibration data points from at least three telescopes must be available, while for an amplitude and phase self-calibration data points from at least four telescopes must be available.

On a completely cleaned data set, model fitting of VLBI data can be used to obtain Gaussian distribution models of the emission regions within the jet, leading to a model that is much simpler and therefore, it is better suitable to study the structure and the time evolution of a source.

To produce plots and do further calculations, such as linear regression, the Interactive Spectral Interpretation System (`ISIS`) (Houck and DeNicola 2000) is used in this thesis.

2. Results of Previous Observations of PKS 0521−365

According to D'Ammando et al. (2015) PKS 0521−365 is an AGN with uncertain classification. Due to the broad emission lines in the optical and UV bands, the steep radio spectrum, the core dominance and the γ-ray properties, they pointed out, that it can be classified as an intermediate object between BLRG and steep spectrum radio quasars (SSRQ). Otherwise, Falomo et al. (2009) and Leon et al. (2016) classify PKS 0521−365 as a BL Lac object.

PKS 0521−365 has a redshift of $z = 0.056$ (D'Ammando et al. 2015). At this distance $1\,\mathrm{mas} = 1\,\mathrm{pc}$.

Very Large Array (VLA) radio observations at 15 GHz, published by Falomo et al. (2009), and ALMA observations (Leon et al. 2016) show a strongly beamed radio jet and a Hot Spot at the counterjet side, detected at $8''$ from the core. Leon et al. (2016) also detected the presence of a weak counterjet, symmetric to the radio jet.

2.1. Viewing Angle

Leon et al. (2016) use the ALMA observations mentioned above to estimate the emission ratio of the jet and the counterjet and found that $R = 10.2$. Using Equation (1.1.14) they compute a range for the viewing angle. To match the PKS 0521−365 ratio it appears that the viewing angle must be in the range $16° \leq \phi \leq 38°$ with a moderate bulk velocity of $0.45 \leq \beta \leq 0.55$, leading to a Lorentz factor of $1.1 \leq \gamma \leq 1.2$ and a Doppler factor of $1.3 \leq \delta \leq 1.7$.

These values are similar to the results of Pian et al. (1996), namely a Lorentz factor of the plasma responsible for the radio jet of $\gamma = 1.2 \pm 0.1$ and a viewing angle of $\phi = 30° \pm 6°$, leading to a Doppler factor of $\delta \approx 1.5$.

Otherwise, D'Ammando et al. (2015) suggest a viewing angle between 6° and 15° by analyzing the spectral energy distribution (SED) of PKS 0521−365. For this purpose, they use, amongst others, γ-ray-data detected by the Large Area Telescope on board the Fermi Gamma-ray Space Telescope satellite (*Fermi*/LAT). These observations show that PKS 0521−365 has been quite active since 2009 September. In 2010 January, an increase of the γ-ray flux was observed, followed by a significant flaring activity between 2010 June and 2012 February (see Fig. 2.1).

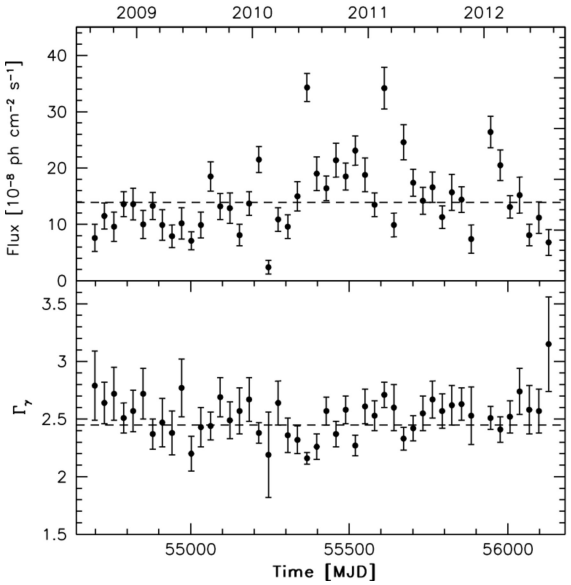

Figure 2.1.: The $0.1 - 100\,\mathrm{GeV}$ flux showing the flaring activity between 2010 June and 2012 February of PKS 0521−365 (top panel) and the photon index from a power-law model (bottom panel). The dashed line in both panels represents the mean value. Taken from D'Ammando et al. (2015).

2.2. Previous Kinematic Analysis

Tingay and Edwards (2002) executed a kinematic analysis by using data of VLBI observations with the Very Long Baseline Array (VLBA) of the National Radio Astronomy Observatory (NRAO) and with the southern hemisphere VLBI Experiment (SHEVE) at 4.9 GHz and 8.4 GHz. These data are listed in Table 2.1 and Table 2.2. Figure 2.2 illustrates the position of these components as a function of time and shows that the components C2 and C3 are consistent with stationary features without significant motion. But, the largest possible apparent speed is $\beta_{\mathrm{app}} = 1.2$ for the component C2 ($< 0.38\,\mathrm{mas\,yr^{-1}}$).

Tingay and Edwards (2002) also compute the brightness temperature of the core, which is in the range $6^{+\mathrm{inf}}_{-5} \cdot 10^{11}\,\mathrm{K}$, and estimate the jet to counterjet surface brightness ratio $R > 20$ by using the peak brightness of the jet side (corresponding to component C1) to the peak noise in the images.

The Doppler factor constraints by Ghisellini et al. (1993) ($\delta > 1$) and Dondi and Ghisellini (1995) ($\delta > 1.3$), which are lower limits, and the constraints on R and β_{app} from Tingay and Edwards (2002) are illustrated in Fig. 2.3, which shows the region of the $\beta - \phi$ plane that satisfies these observational constraints (shaded in gray). To calculate the jet to counterjet surface brightness ratio, Tingay and Edwards (2002) use $p = 3 - \alpha$ as the exponent in the expression for R (Equation(1.1.14)), because they

suppose that the emission is not due to a continuous jet but to discrete components. For α they used the measured spectral index for component C1, namely $\alpha = -0.6$. If the constraints of Pian et al. (1996) (see Sect. 2.1) are also considered (Fig. 2.3, boxed area), the allowed region of the $\beta - \phi$ plane is diminished to the area shaded in black. According to Tingay and Edwards (2002) Fig. 2.3 shows that higher-sensitivity VLBI observations, which might lead to stronger constraints on R, could rule out the entire area allowed by Pian et al. (1996) and therefore test the result of Pian et al. (1996).

Table 2.1.: Model fit parameters for the 4.9 GHz SHEVE and VLBA observations of PKS 0521−365, according to Tingay and Edwards (2002).

S	R	Θ	a_{maj}	ratio	P.A.	ID
[Jy]	[mas]	[deg]	[mas]		[deg]	
(1)	(2)	(3)	(4)	(5)	(6)	(7)
1992-11-23:						
1.3	0.0	0.0	0.0	0.0	0.0	Core
0.2	7.8	−54.6	0.0	0.0	0.0	C2
1993-02-15:						
1.8	0.0	0.0	0.0	0.0	0.0	Core
0.3	3.3	−41.1	1.4	0.0	−21.7	C3
0.2	8.6	−45.2	3.8	0.0	−51.4	C2
1993-05-14:						
1.9	0.0	0.0	0.0	0.0	0.0	Core
0.2	2.5	−50.5	0.7	0.0	−52.0	C3
0.2	9.4	−44.7	3.7	0.0	−55.1	C2
1998-06-17:						
1.3	0.0	0.0	2.7	0.0	9.2	Core
0.2	5.6	−52.4	12.7	0.0	−39.1	C2/C3
0.4	27.5	−46.5	11.9	0.4	−42.4	C1
2000-04-23:						
1.2	0.0	0.0	2.0	0.0	−43.8	Core
0.1	7.6	−57.2	12.6	0.0	−37.2	C2/C3
0.5	26.8	−47.0	11.4	0.2	−52.3	C1

Note: Col.(1): S is the flux density of the component. Col.(2): R is the angular distance of the component from the designated phase center. Col.(3): Θ is the position angle of the component centroid from the designated phase center in degrees east of north. Col.(4): a_{maj} is the major axis of the component. Col.(5): ratio of the component minor axis to major axis. Col.(6): P.A. is the position angle of the component major axis in degrees east of north. Col.(7): ID is the component identification.

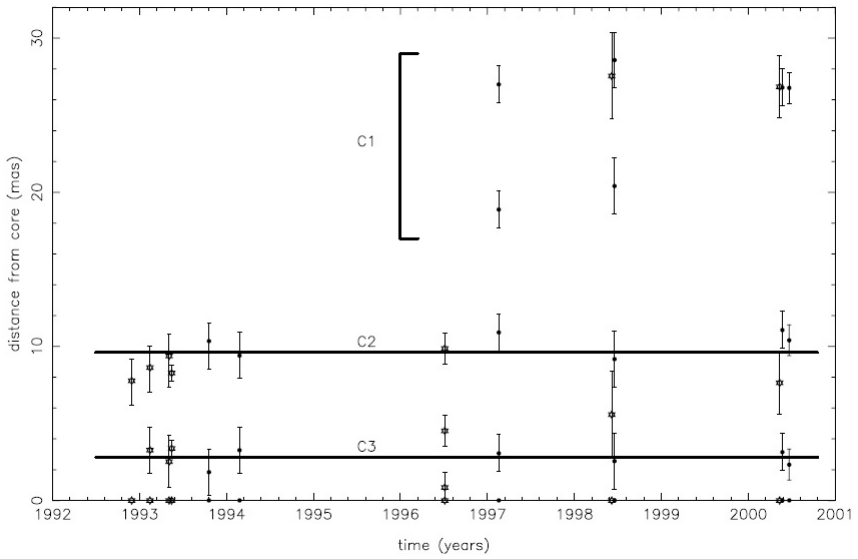

Figure 2.2.: Position of the components listed in Table 2.1 and Table 2.2 as a function of time. Stars denote the 4.9 GHz data and filled circles denote the 8.4 GHz data. Taken from Tingay and Edwards (2002).

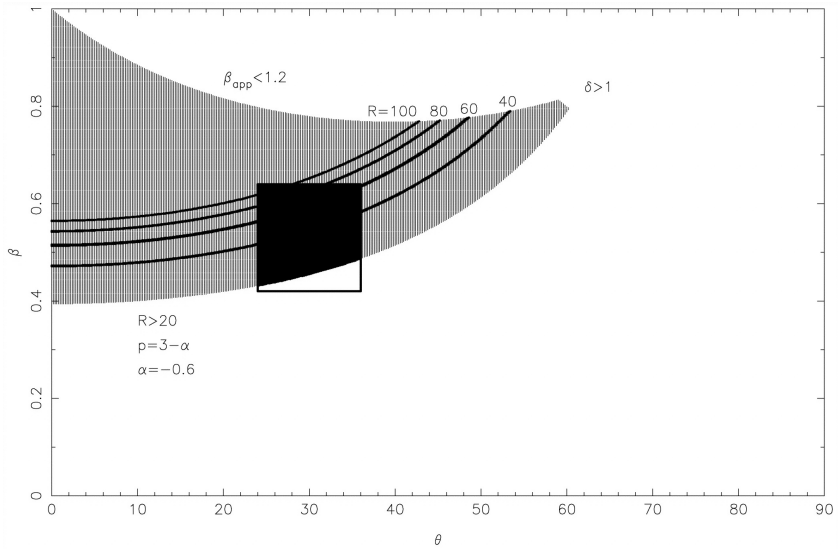

Figure 2.3.: Region of the $\beta - \phi$ plane (here ϕ is called θ) that satisfies the constraints $\delta > 1$, $\beta_{\rm app} < 1.2$, $R > 20$ is shaded in gray. The region of the plane that satisfies the constraints of Pian et al. (1996) is shown as the boxed area. Also indicated are the loci corresponding to various values of R, for comparison to the current constraints. Taken from Tingay and Edwards (2002).

Table 2.2.: Model fit parameters for the 8.4 GHz SHEVE and VLBA observations of PKS 0521−365, according to Tingay and Edwards (2002).

S	R	Θ	a_{maj}	ratio	P.A.	ID
[Jy]	[mas]	[deg]	[mas]		[deg]	
(1)	(2)	(3)	(4)	(5)	(6)	(7)
1993-10-21:						
1.6	0.0	0.0	0.0	0.0	0.0	Core
0.4	1.8	−40.5	0.0	0.1	−50.0	C3
0.1	10.3	−44.4	1.6	0.6	−13.2	C2
1994-02-26:						
1.6	0.0	0.0	1.7	0.4	−54.7	Core
0.1	3.3	−19.3	1.2	0.0	−34.4	C3
0.2	9.4	−44.9	5.1	0.2	−62.3	C2
1997-02-17:						
1.6	0.0	0.0	1.2	0.7	−52.8	Core
0.1	3.1	−56.1	2.1	0.2	14.9	C3
0.1	10.9	−43.6	7.7	0.0	−62.7	C2
0.1	18.9	−47.4	2.3	0.2	−13.7	C1
0.2	27.0	−47.8	7.0	0.4	−31.8	C1
1998-06-17:						
1.7	0.0	0.0	1.0	0.0	−20.5	Core
0.1	2.6	−54.3	10.9	0.0	22.2	C3
0.05	9.2	−48.4	4.5	0.3	−58.9	C2
0.1	20.4	−45.7	4.2	0.9	76.9	C1
0.2	28.6	−47.8	7.1	0.4	−35.3	C1
2000-04-23:						
1.3	0.0	0.0	1.5	0.5	11.1	Core
0.1	3.1	−54.4	1.4	1.0	−104.0	C3
0.1	11.1	−50.3	2.4	1.0	−81.9	C2
0.3	26.8	−47.4	12.6	0.3	−45.8	C1
2000-05-25:						
1.6	0.0	0.0	0.9	0.0	−58.6	Core
0.1	2.3	−61.9	1.7	0.4	84.0	C3
0.05	10.4	−56.4	3.5	0.0	43.2	C2
0.3	26.8	−48.1	11.6	0.1	−49.4	C1

Note: Columns same as Table 2.1.

3. TANAMI Observations of PKS 0521−365

3.1. Imaging and Model fitting

Nine epochs of TANAMI VLBI observations at 8.4 GHz of PKS 0521−365 were investigated between 2007 November and 2012 September. Imaging and model fitting these epochs as well as analyzing the time evolution of the jet is the main part of this thesis. This Section will focus on the description of the received images of these nine epochs.

The (u, v)-plane coverages of the epochs are presented in Sect. A.1. Looking at this plots, it is noticeable that in 2008 August (Fig. A.3) there are only very little data at the longest baselines and that in 2010 March (Fig. A.5) there is a lack of the longest baselines, meaning that only baselines up to around 50 Mλ were available. This was due to a big earthquake.

The images of the nine epochs were produced using the `clean` algorithm within `DIFMAP` with natural weighting. Thereby, windows were only set in the direction of the jet, but not on the possible counterjet side, meaning that the algorithm was only allowed to clean in the jet direction. The images, produced in this way, are shown in Sect. A.2 Fig. A.10 until Fig. A.18 and the image parameters are listed in Table 3.1. The plots show a knotty jet structure with an extension of around 80 mas which equates to 80 pc. The beam of the 2008 August epoch (Fig. A.12) is a little larger as the beams of the other epochs, apart from the 2010 March epoch, this is due to the lack of data at the longest baselines mentioned above, which leads to a worse resolution, compared to the other epochs. The complete lack of baselines above 50 Mλ at the 2010 March epoch leads to a very big beam and a very bad resolution compared to the other epochs, but the image of this epoch (Fig. A.14) shows a nice continuous jet structure which makes model fitting easier.

Therefore, all nine epochs were imaged with a Gaussian taper of 0.1 at a radius of 50 Mλ which means, according to Ojha et al. (2010), that the visibility data of baselines longer than 50 Mλ were down weighted to 10 %. Now, all images of all epochs show a countinuous jet structure. These so called tapered-images are presented in Sect. A.2 Fig. A.19 until Fig. A.27 and the appropriate image parameters are listed in Table 3.2. This images were used for model fitting the jet.

For the kinematic analysis the tapered-images were still restored with the same beam, computed with the biggest minor and major axis of all nine beams of all nine epochs.

Table 3.1.: Details of observation and image parameters.

Date YYYY-MM-DD (1)	Array Configuration (2)	$S_{\rm tot}$ [Jy] (3)	$S_{\rm peak}$ [Jy/beam] (4)	$\sigma_{\rm rms}$ [mJy/beam] (5)	$b_{\rm maj}$ [mas] (6)	$b_{\rm min}$ [mas] (7)	P.A. [deg] (8)
2007-11-10	PA-CATW113-MP-HO-CD-HH	1.57	0.94	0.34	1.04	0.25	1.72
2008-03-28	PA-CATW104-MP-HO-CD-HH-DSS43	1.58	0.95	0.30	1.48	0.28	−0.54
2008-08-08	PA-CATW104-MP-HO-CD-HH-DSS45	1.87	1.45	0.25	1.65	0.82	−5.39
2009-02-23	AT-CD-DSS43-DSS45-HO-MP-OH-PA-TC	1.62	0.88	0.49	1.14	0.26	22.35
2010-03-12	AT-CD-HO-MP-PA-TI	1.63	1.31	0.21	3.15	1.78	83.65
2010-07-24	AT-CD-HO-MP-PA-TC-TI	1.94	1.37	0.31	1.62	0.38	13.75
2011-04-01	AT-CD-DSS43-HH-HO-MP-PA-TC-WW	2.90	1.80	0.83	1.23	0.25	−1.20
2011-11-13	AT-CD-HH-HO-MP-PA-TC-TD-TI-WW	2.73	1.57	0.55	1.28	0.19	−1.09
2012-09-16	AK-AT-CD-HH-HO-KE-PA-TC-TD-TI	2.18	1.58	0.55	1.33	0.32	4.20

Note: Col.(1): Date of observation. Col.(2): AT: ATCA, CD: Ceduna, HO: Hobart, MP: Mopra, OH: O'Higgins, PA: Parkes, TC: TIGO, DSS43 & 45: Tidbinbilla (70 m&34 m), KE: Katherine, HH: Hartebeesthoek, AK: ASKAP. Col.(3): $S_{\rm tot}$ is the total flux density. Col.(4): $S_{\rm peak}$ is the peaked flux density of the core. Col.(5): $\sigma_{\rm rms}$ is the noise level. Col.(6): $b_{\rm maj}$ is the semi major axis of the beam. Col.(7): $b_{\rm min}$ is the semi minor axis of the beam. Col.(8): P.A. is the position angle of the beam.

The so received restored-images are shown in Fig. 3.2 and the image parameters are listed in Table 3.3. Now, the images can be compared with each other, because they have all the same beam size. One can see an enormous increase in the total flux density and also in the peaked flux density since 2010 July, corresponding to the γ-ray flaring activity detected by *Fermi*/LAT between 2010 June and 2012 February shown in Fig. 2.1 (D'Ammando et al. 2015).

Because of the noise features that can be seen in Fig. A.10 until Fig. A.18, one could think that there must be more flux density to be cleaned. Therefore, and due to the detection of a weak counterjet by the ALMA observations presented by Leon et al. (2016) (see also Sect. 2), it was tried to produce images with a counterjet. Hence, in `DIFMAP` windows were also set on the counterjet side nearly symmetric to the windows on the jet side, meaning that now the `clean` algorithm was also allowed to clean in the counterjet direction, but not only in the jet direction. While not representing a statistically competitive model representation of the measured visibilities, such a jet-counterjet model cannot be fully excluded given the sparse (u, v)-plane coverage. The jet-counterjet images lead to the lowest limit of the flux density ratio between the jet and the counterjet possible of $R \gtrsim 4$, estimated by using the flux densities of the whole jet and counterjet structure.

For model fitting the nine TANAMI epochs the produced tapered-images were used. Thereby, the core of each epoch was fitted by an elliptical Gaussian component, while the jet structures were fitted with circular Gaussian components. In Fig. 3.1 the major axes, or rather the radii, of the jet components are plotted as a function of the distance

Table 3.2.: Image parameters of the tapered-images.

Date YYYY-MM-DD (1)	Array Configuration (2)	$S_{\rm tot}$ [Jy] (3)	$S_{\rm peak}$ [Jy/beam] (4)	$\sigma_{\rm rms}$ [mJy/beam] (5)	$b_{\rm maj}$ [mas] (6)	$b_{\rm min}$ [mas] (7)	P.A. [deg] (8)
2007-11-10	PA-CATW113-MP-HO-CD-HH	1.58	1.29	0.53	3.51	2.14	−66.46
2008-03-28	PA-CATW104-MP-HO-CD-HH-DSS43	1.61	1.22	0.23	4.42	2.14	−60.73
2008-08-08	PA-CATW104-MP-HO-CD-HH-DSS45	1.87	1.57	0.21	3.74	2.21	−77.92
2009-02-23	AT-CD-DSS43-DSS45-HO-MP-OH-PA-TC	1.75	1.31	0.44	2.90	2.27	70.47
2010-03-12	AT-CD-HO-MP-PA-TI	1.63	1.31	0.21	3.15	1.78	83.65
2010-07-24	AT-CD-HO-MP-PA-TC-TI	1.97	1.74	0.21	4.72	2.29	76.20
2011-04-01	AT-CD-DSS43-HH-HO-MP-PA-TC-WW	2.94	2.69	0.70	3.36	2.43	−79.64
2011-11-13	AT-CD-HH-HO-MP-PA-TC-TD-TI-WW	2.79	2.51	0.90	4.29	2.16	−63.60
2012-09-16	AK-AT-CD-HH-HO-KE-PA-TC-TD-TI	2.18	1.94	0.31	2.39	2.09	82.51

Note: Columns same as Table A.15. The images where done by setting a taper at 50 Mλ.

Table 3.3.: Image parameters of the restored-images.

Date YYYY-MM-DD (1)	Array Configuration (2)	$S_{\rm tot}$ [Jy] (3)	$S_{\rm peak}$ [Jy/beam] (4)	$\sigma_{\rm rms}$ [mJy/beam] (5)	$b_{\rm maj}$ [mas] (6)	$b_{\rm min}$ [mas] (7)	P.A. [deg] (8)
2007-11-10	PA-CATW113-MP-HO-CD-HH	1.58	1.31	0.54	5.23	3.26	93.97
2008-03-28	PA-CATW104-MP-HO-CD-HH-DSS43	1.61	1.23	0.24	5.23	3.26	93.97
2008-08-08	PA-CATW104-MP-HO-CD-HH-DSS45	1.87	1.58	0.22	5.23	3.26	93.97
2009-02-23	AT-CD-DSS43-DSS45-HO-MP-OH-PA-TC	1.75	1.38	0.47	5.23	3.26	93.97
2010-03-12	AT-CD-HO-MP-PA-TI	1.63	1.38	0.19	5.23	3.26	93.97
2010-07-24	AT-CD-HO-MP-PA-TC-TI	1.97	1.76	0.22	5.23	3.26	93.97
2011-04-01	AT-CD-DSS43-HH-HO-MP-PA-TC-WW	2.94	2.69	0.72	5.23	3.26	93.97
2011-11-13	AT-CD-HH-HO-MP-PA-TC-TD-TI-WW	2.79	2.51	0.92	5.23	3.26	93.97
2012-09-16	AK-AT-CD-HH-HO-KE-PA-TC-TD-TI	2.18	2.01	0.32	5.23	3.26	93.97

Note: Columns same as Table A.15. The images were produced by restoring the tapered-images by the same mean beam.

between them and the corresponding core component. On the upper left panel one can see that the major axes of some components diverges underneath a value of 10^{-6} mas, meaning that these components were unresolved. Another problem of the diverging components is that such small major axes lead, according to Equation (1.1.7), to unphysically high brightness temperatures. Furthermore, the diverging components would lead to an overvalued accuracy of the jet speed, because, as pointed out further down in Sect. 3.2, the uncertainties of the speed depends on the major axes of the moving components. To manage these problems, the diverging major axes were set to a value that physically makes sense. Therefore, the mean major axis as a function of the distance was calculated by linear regression neglecting the diverging components (see the dashed line on the upper right panel of Fig. 3.1). Then, the major axes of all components,

that major axis lies underneath a value of 0.1 mas, were set to the computed value of the mean major axis (see bottom panel of Fig. 3.1). This is acceptable, if a narrow conical jet model (Blandford and Königl 1979) is supposed, meaning that the radii of the circular Gaussian components must increase linear with the distance. The corrected jet components, together with all other components, are listed in Table 3.4.

With this components a lower limit for the jet to counterjet brightness ratio can be computed. Therefore, the flux density of the jet was estimated by the brightest component of all nine epochs, namely $S_{\mathrm{jet}} = 0.21\,\mathrm{Jy}$ for component C8 of the 2009 February epoch, while an upper limit for the flux density of the counterjet was estimated as five times the noise level of that epoch. According to Böck (2012) the noise level was calculated in `DIFMAP` by selecting a region in the image which only includes noise. It would have been necessary to make sure that no jet components are included in this selected area. This method leads to a noise level of $\sigma_{\mathrm{rms}} = 0.00044\,\mathrm{Jy/beam}$ which leads to a flux density of $S_{\mathrm{counter}} = 0.0022\,\mathrm{Jy}$. So, the ratio becomes $R > 95$.

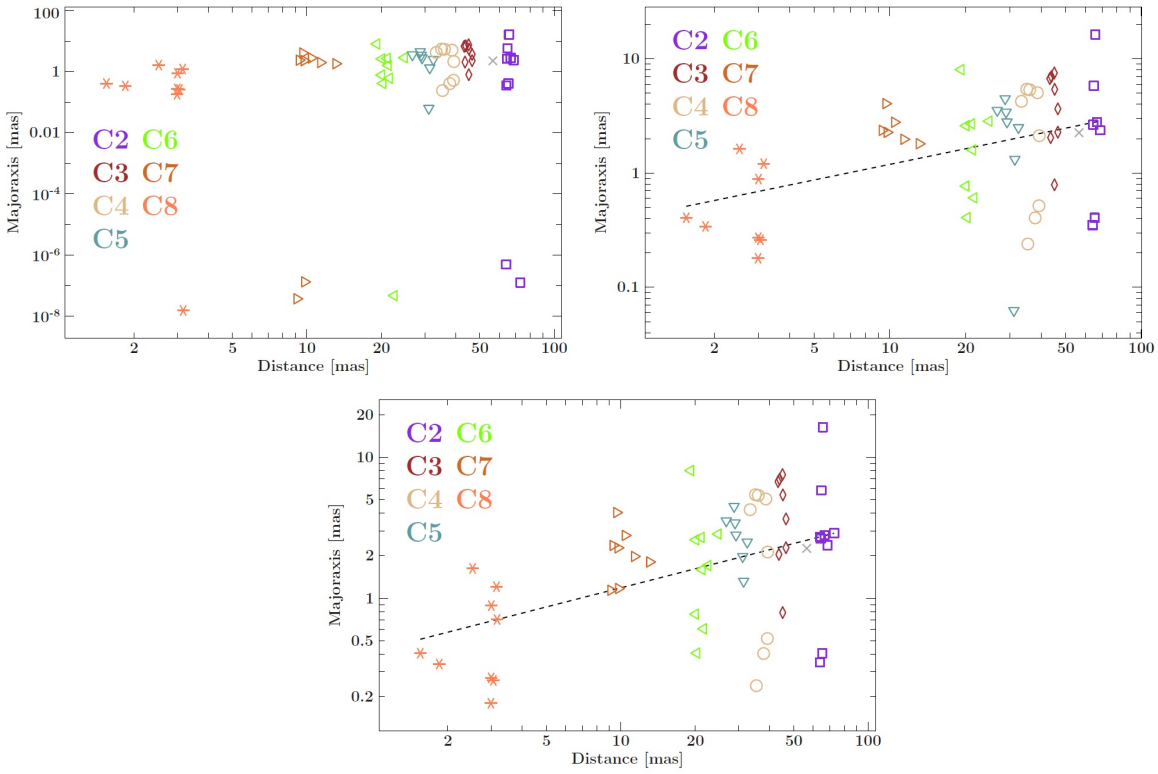

Figure 3.1.: Upper left panel: Major axes of the jet components as a function of the distance to the core component. Six components diverge. Upper right panel: The dashed line represents the mean major axis as a function of the distance computed by linear regression, neglecting the diverging components. Bottom panel: Components that have major axes underneath 0.1 mas were shifted onto the dashed line.

Table 3.4.: Model fit parameters for the TANAMI observations of PKS 0521−365.

S [Jy] (1)	R [mas] (2)	Θ [deg] (3)	a_{maj} [mas] (4)	ratio (5)	P.A. [deg] (6)	ID (7)
2007-11-10:						
1.18	0.056	−37.40	0.25	$8.02 \cdot 10^{-9}$	−47.23	Core
0.15	2.58	−51.49	1.63	1.00	−178.48	C8
0.0084	9.18	−43.37	1.14*	1.00	−170.93	C7
0.048	20.34	−47.29	0.41	1.00	−164.85	C6
0.11	32.51	−45.68	2.50	1.00	−164.27	C5
0.020	37.88	−50.18	0.41	1.00	−175.44	C4
0.030	46.61	−43.90	2.28	1.00	−141.56	C3
0.018	65.35	−45.19	0.41	1.00	−167.10	C2
2008-03-28:						
1.16	0.030	−159.03	0.54	0.27	−9.77	Core
0.075	2.98	−47.41	0.18	1.00	−169.16	C8
0.060	9.79	−42.83	1.17*	1.00	−164.16	C7
0.027	21.58	−39.95	0.61	1.00	−172.56	C6
0.080	26.71	−44.86	3.53	1.00	−177.89	C5
0.12	38.59	−47.86	5.06	1.00	177.62	C4
0.019	45.12	−46.14	0.79	1.00	−175.79	C3
0.059	65.64	−44.38	16.30	1.00	−169.73	C2
2008-08-08:						
1.52	0.014	−107.93	0.13	0.00	−82.99	Core
0.082	3.00	−50.16	0.27	1.00	−159.78	C8
0.069	10.45	−47.43	2.79	1.00	−173.38	C7
0.021	22.53	−41.30	1.70*	1.00	−169.56	C6
0.066	28.73	−44.86	4.47	1.00	−154.41	C5
0.072	35.04	−47.13	5.42	1.00	−148.38	C4
0.023	46.56	−45.37	3.65	1.00	−170.62	C3
0.016	72.88	−43.21	2.89*	1.00	−176.87	C2
2009-02-23:						
1.24	0.030	−116.32	0.34	0.51	22.25	Core
0.21	3.16	−48.48	1.21	1.00	−178.32	C8
0.058	13.11	−45.61	1.81	1.00	−176.95	C7
0.044	24.77	−42.44	2.85	1.00	−170.76	C6
0.023	31.41	−48.54	1.32	1.00	−174.34	C5
0.027	35.38	−51.98	0.24	1.00	−167.54	C4
0.10	43.26	−46.00	6.71	1.00	−125.13	C3
0.049	64.37	−50.06	2.65	1.00	−172.95	C2
2010-03-12:						
1.33	0.053	149.90	1.40	$8.18 \cdot 10^{-9}$	−65.91	Core
0.079	2.95	−56.64	0.89	1.00	−175.13	C8
0.048	9.58	−55.48	4.05	1.00	−169.82	C7
0.023	21.28	−40.33	1.59	1.00	−178.48	C6
0.017	28.94	−43.39	3.42	1.00	−172.88	C5
0.038	33.31	−46.87	4.24	1.00	−150.81	C4
0.055	43.83	−48.78	6.98	1.00	−174.18	C3
0.015	56.44	−49.25	2.26	1.00	−172.02	—
0.025	66.63	−49.84	2.80	1.00	−180.00	C2
2010-07-24:						
1.70	0.011	−122.93	0.063	0.00	87.87	Core
0.080	3.06	−53.08	0.26	1.00	−175.44	C8
0.051	9.76	−49.42	2.27	1.00	−161.69	C7
0.014	20.05	−37.30	0.77	1.00	−162.29	C6
0.040	29.23	−43.59	2.80	1.00	−167.88	C5
0.042	35.98	−45.25	5.36	1.00	−175.02	C4
0.034	45.08	−45.23	7.52	1.00	−175.62	C3
0.012	63.90	−46.25	2.72*	1.00	−173.75	C2
2011-04-01:						
2.60	0.018	−54.98	0.17	0.31	−27.55	Core
0.099	1.57	−31.67	0.41	1.00	−158.74	C8
0.13	19.18	−46.17	8.04	1.00	−175.94	C6
0.020	39.29	−48.67	2.12	1.00	−172.21	C4
0.056	45.24	−46.09	5.40	1.00	180.00	C3
0.029	68.59	−47.45	2.37	1.00	−176.28	C2
2011-11-13:						
2.45	0.044	−47.88	0.11	$8.93 \cdot 10^{-9}$	−73.27	Core
0.089	1.89	−51.72	0.34	1.00	180.00	C8
0.051	11.41	−50.46	1.98	1.00	178.88	C7
0.068	20.13	−42.51	2.60	1.00	180.00	C6
0.017	31.17	−51.08	1.97*	1.00	−166.53	C5
0.011	39.19	−46.44	0.52	1.00	−34.07	C4
0.047	43.63	−49.58	2.04	1.00	−20.96	C3
0.062	64.75	−45.70	5.82	1.00	180.00	C2
2012-09-16:						
1.91	0.013	−44.05	0.35	0.35	5.29	Core
0.14	3.18	−52.08	0.71*	1.00	−173.00	C8
0.073	9.33	−42.04	2.37	1.00	180.00	C7
0.036	21.15	−48.77	2.70	1.00	−160.51	C6
0.022	63.97	−48.61	0.35	1.00	−53.84	C2

Note: Columns same as Table 2.1. Components labeled with * are the diverging components that are increased to the given value.

3.2. Kinematic Analysis

To analyze the movement of the components, their position relative to the core component was studied. Their time evolution is shown in Fig. 3.2, where the restored-images of the jet are plotted overlain by the Gaussian components.

The speed of the jet components was determined by linear regression of the distance to the core component and by vectorial linear regression, where first the speeds in both x and y directions were computed separately and then the overall speed of the component was computed using this two speeds. Therefor, the uncertainties of the position of the components were estimated by the semi major axis of the corresponding component. All computed speeds for both methods are listed in Table 3.5 and the distance over time is plotted in Fig. 3.3, where the dashed lines are computed by the vectorial method of the linear regression, similar to the dashed lines in Fig. 3.2.

One can see that there are some components with negative speeds, even within the uncertainties. Especially for the vectorial method there are only three components with positive speeds within the uncertainties. This would imply that the jet components move back to the core component which was very unphysical. But, if the data presented by Tingay and Edwards (2002) are taken into account, this problem can be solved. Furthermore, with this approach one can investigate the time evolution of PKS 0521−365 during a period of nearly 20 years from 1992 November until 2012 September.

There are two possible versions to connect the data of Tingay and Edwards (2002) with the TANAMI data analyzed in this thesis. In both variations the components C2

Table 3.5.: Apparent speed of the components relative to the core component in the period between 2007-11-10 and 2012-09-16.

Component	$v_{\mathrm{app,dist}}$ $[\mathrm{mas\,yr^{-1}}]$	$\beta_{\mathrm{app,dist}}$	$v_{\mathrm{app,vec}}$ $[\mathrm{mas\,yr^{-1}}]$	$\beta_{\mathrm{app,vec}}$
(1)	(2)	(3)	(4)	(5)
C2	-0.291 ± 0.055	-1.10 ± 0.21	-0.84 ± 0.10	-3.18 ± 0.39
C3	-0.46 ± 0.28	-1.7 ± 1.1	-0.87 ± 0.55	-3.3 ± 2.1
C4	0.459 ± 0.080	1.74 ± 0.30	0.84 ± 0.16	3.17 ± 0.60
C5	-0.07 ± 0.33	-0.3 ± 1.3	-0.51 ± 0.59	-1.9 ± 2.2
C6	-0.04 ± 0.13	-0.15 ± 0.49	-0.77 ± 0.19	-2.92 ± 0.72
C7	0.22 ± 0.20	0.81 ± 0.74	0.28 ± 0.20	1.07 ± 0.74
C8	-0.216 ± 0.039	-0.82 ± 0.15	-0.224 ± 0.064	-0.85 ± 0.24

Note: Col.(1): Component ID. Col.(2): $v_{\mathrm{app,dist}}$ is the apparent speed computed by linear regression over the distance relative to the core component. Col.(3): $\beta_{\mathrm{app,dist}}$ is the relative apparent speed corresponding to $v_{\mathrm{app,dist}}$. Col.(4): $v_{\mathrm{app,vec}}$ is the apparent speed computed by vectorial linear regression. Col.(5): $\beta_{\mathrm{app,vec}}$ is the relative apparent speed corresponding to $v_{\mathrm{app,vec}}$.

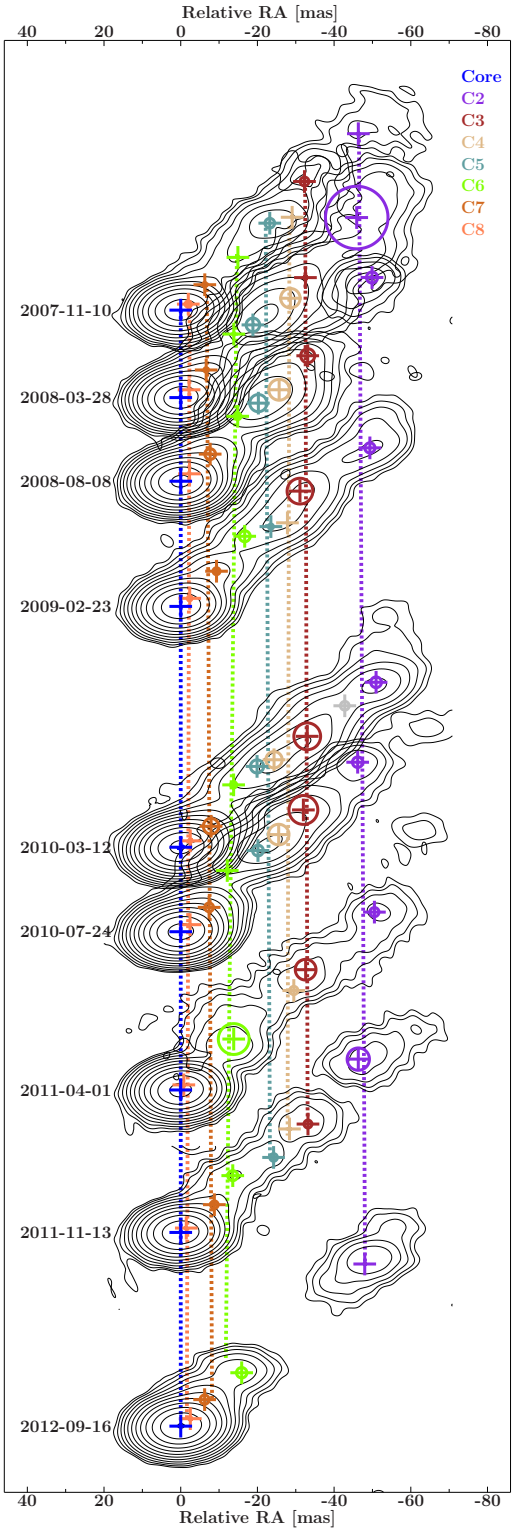

Figure 3.2.: Time evolution of the component position relative to the position of the core component. The restored-images were overlaid with the components listed in Table 3.4. The dashed lines are plotted by linear regression of the distance as a function of the time. The contours begin at 3σ and increase logarithmically by a factor of 2.

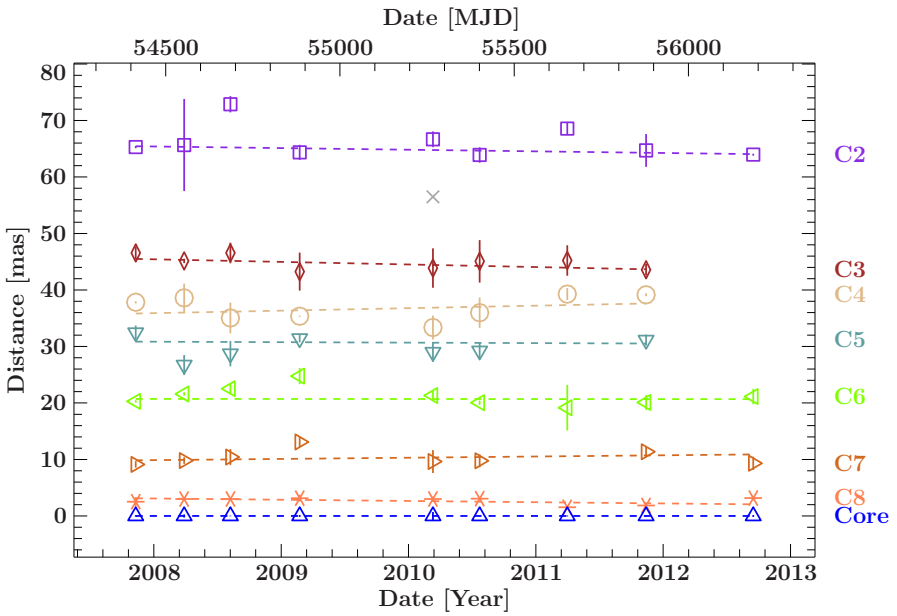

Figure 3.3.: Distance of the jet components relative to the core component plotted over time. The dashed lines are computed by vectorial linear regression. Their gradients represents the speed of the corresponding component. The error bars are estimated by the semi major axis of the corresponding jet component.

and C3 of Tingay and Edwards (2002) can be identified with the components C7 and C8 of the TANAMI data. But, for the component C1 of Tingay and Edwards (2002) there are two different possibilities to connect it with the TANAMI data. On the one hand side, it can be identified with component C6 of the TANAMI data. On the other hand side, it can be split into two components identified with the two components C5 and C6 of the TANAMI data. The computed speeds for both variants are listed in Table 3.6. Here, the speeds were calculated by linear regression of the distance to the core component over time. The uncertainties of the position of the components were also estimated by the semi major axis of the corresponding component. The distance over time is plotted in Fig. 4.1 for both versions.

Now, only the outer components C2 and C3 have negative speeds, even within the uncertainties. But, these components can be neglected, because they belong to very diffuse regions of the jet. Indeed, the speed of component C8 is also negative, even within the uncertainties, but it is very close to zero. All other speeds are positive within the uncertainties and also very close to zero. Only the speed of component C4 is incompatible with zero. So, no motion is a good description.

Table 3.6.: Apparent speed of the components relative to the core component in the period between 1992-11-23 and 2012-09-16.

Component	$v_{\mathrm{app,var1}}$ [mas yr^{-1}]	$\beta_{\mathrm{app,var1}}$	$v_{\mathrm{app,var2}}$ [mas yr^{-1}]	$\beta_{\mathrm{app,var2}}$
(1)	(2)	(3)	(4)	(5)
C2	-0.291 ± 0.055	-1.10 ± 0.21	-0.291 ± 0.055	-1.10 ± 0.21
C3	-0.46 ± 0.28	-1.7 ± 1.1	-0.46 ± 0.28	-1.7 ± 1.1
C4	0.459 ± 0.080	1.74 ± 0.30	0.459 ± 0.080	1.74 ± 0.30
C5	-0.07 ± 0.33	-0.3 ± 1.3	0.21 ± 0.16	0.80 ± 0.59
C6	-0.021 ± 0.070	-0.08 ± 0.26	0.076 ± 0.074	0.29 ± 0.28
C7	0.057 ± 0.038	0.22 ± 0.14	0.057 ± 0.038	0.22 ± 0.14
C8	-0.023 ± 0.014	-0.087 ± 0.054	-0.023 ± 0.014	-0.087 ± 0.054

Note: Col.(1): Component ID. Col.(2): $v_{\mathrm{app,var1}}$ is the apparent speed computed by linear regression over the distance relative to the core component, using the TANAMI data and the data of Tingay and Edwards (2002). The component C1 of Tingay and Edwards (2002) is identified with component C6 of the TANAMI data. Col.(3): $\beta_{\mathrm{app,var1}}$ is the relative apparent speed corresponding to $v_{\mathrm{app,var1}}$. Col.(4): $v_{\mathrm{app,var2}}$ is the apparent speed computed by linear regression over the distance relative to the core component, using the TANAMI data and the data of Tingay and Edwards (2002). The component C1 of Tingay and Edwards (2002) is split into two components which are identified with components C5 and C6 of the TANAMI data. Col.(5): $\beta_{\mathrm{app,var2}}$ is the relative apparent speed corresponding to $v_{\mathrm{app,var2}}$.

3.3. Brightness Temperature of the Core Component

The ratio of the major to the minor axis of the core component given in Table 3.4 shows that most minor axes diverge. Because the brightness temperature is inversely proportional to these axes (see Equation (1.1.7)), this leads to unphysically high values of the brightness temperature of the core component. Hence, a resolution limit for the axes of the core component was computed for each epoch. According to Kovalev et al. (2005) the minimum resolvable size θ_{lim} of a Gaussian component is given by

$$\theta_{\mathrm{lim}} = b_{\psi} \sqrt{\frac{4 \ln 2}{\pi} \ln \left(\frac{SNR}{SNR - 1} \right)}, \tag{3.3.1}$$

where b_{ψ} is the half-power beam size measured along an arbitrary position angle ψ and SNR is given by $SNR = \frac{S_{\mathrm{core}}}{\sigma_{\mathrm{core}}}$. Here, σ_{core} is the noise level in the area of the image occupied by the core component and S_{core} is the flux density of the core component. θ_{lim}, corresponding to the position angles of the minor and major axis of the core component, was computed for all epochs. Whenever an axis was smaller than the corresponding θ_{lim}, the component was considered to be unresolved. θ_{lim} was then used as an upper limit to the size of the corresponding axis, leading, according to Equation (1.1.7), to a lower

limit to the brightness temperature T_{B} of the core component. The computed limits to the brightness temperature of the core component are listed in Table 3.7.

Table 3.7.: Brightness temperature of the core.

Date YYYY-MM-DD (1)	S_{core} [Jy/beam] (2)	σ_{core} [mJy/beam] (3)	SNR (4)	θ_{maj} [mas] (5)	θ_{min} [mas] (6)	$\theta_{\mathrm{lim,maj}}$ [mas] (7)	$\theta_{\mathrm{lim,min}}$ [mas] (8)	T_{B} [K] (9)
2007-11-10	1.29	1.28	$1.01 \cdot 10^{3}$	0.126	$1.01 \cdot 10^{-9}$	0.095	0.066	$6.47 \cdot 10^{11}$
2008-03-28	1.22	1.37	$8.88 \cdot 10^{2}$	0.271	0.072	0.081	0.092	$2.14 \cdot 10^{11}$
2008-08-08	1.57	1.78	$8.78 \cdot 10^{2}$	0.065	0.000	0.118	0.070	$8.30 \cdot 10^{11}$
2009-02-23	1.31	1.38	$9.50 \cdot 10^{2}$	0.169	0.085	0.076	0.078	$3.88 \cdot 10^{11}$
2010-03-12	1.31	1.61	$8.15 \cdot 10^{2}$	0.700	$5.72 \cdot 10^{-9}$	0.083	0.064	$1.34 \cdot 10^{11}$
2010-07-24	1.74	0.96	$1.81 \cdot 10^{3}$	0.031	0.000	0.098	0.051	$1.54 \cdot 10^{12}$
2011-04-01	2.69	0.65	$4.14 \cdot 10^{3}$	0.083	0.026	0.039	0.042	$3.37 \cdot 10^{12}$
2011-11-13	2.51	0.32	$7.94 \cdot 10^{3}$	0.057	$5.06 \cdot 10^{-10}$	0.043	0.023	$8.48 \cdot 10^{12}$
2012-09-16	1.94	0.50	$3.92 \cdot 10^{3}$	0.173	0.061	0.032	0.036	$8.26 \cdot 10^{11}$

Note: Col.(1): Date of observation. Col.(2): S_{core} is the peaked flux density of the core. Col.(3): σ_{core} is the noise level of the core. Col.(4): SNR is the ratio $S_{\mathrm{core}}/\sigma_{\mathrm{core}}$. Col.(5): θ_{maj} is the semi major axis of the core. Col.(6): θ_{min} is the semi minor axis of the core. Col.(7): $\theta_{\mathrm{lim,maj}}$ is the resolution limit of the semi major axis. Col.(8): $\theta_{\mathrm{lim,min}}$ is the resolution limit of the semi minor axis. Col.(9): T_{B} is the brightness temperature of the core.

4. Discussion

4.1. Jet Kinematics and Orientation

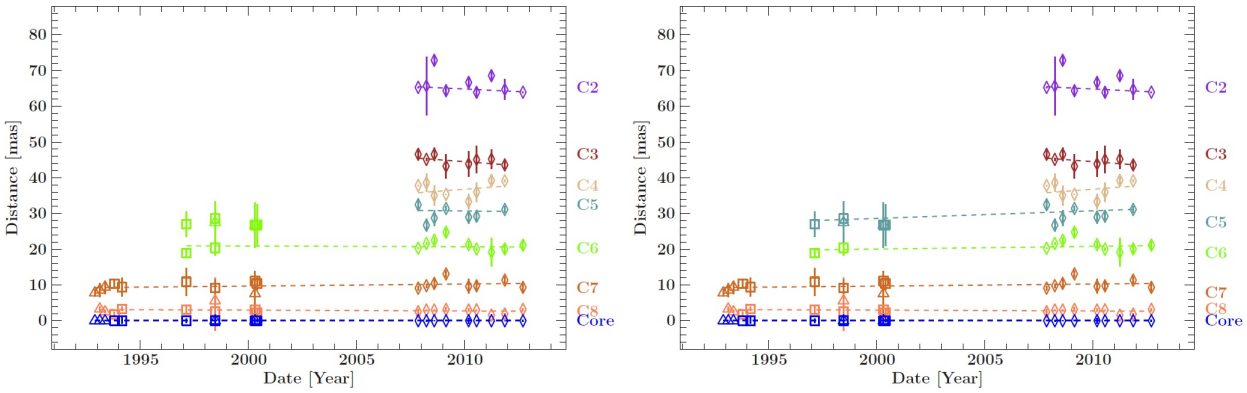

Figure 4.1.: Distance of the jet components relative to the core component plotted as a function of time, using the data of Tingay and Edwards (2002) and the TANAMI data of this thesis. Triangles denote the 4.9 GHz SHEVE and VLBA data, squares denote the 8.4 GHz SHEVE and VLBA data and rhombi denote the 8.4 GHz TANAMI data. The dotted lines represent the linear regression over distance. The error bars are set to half of the major axis as an estimation of the uncertainties for the distance. Shown are two possible versions where the components C2 and C3 of Tingay and Edwards (2002) are in both cases associated with the components C7 and C8 of the TANAMI data. In the left panel the component C1 of Tingay and Edwards (2002) is associated with the component C6 of the TANAMI data. In the right panel the component C1 of Tingay and Edwards (2002) is split into two components associated with the components C6 and C5 of the TANAMI data.

Using the TANAMI data combined with the VLBA and SHEVE data presented by Tingay and Edwards (2002), the largest possible apparent speed is $\beta_{\mathrm{app}} = 2.04$ for component C4 ($< 0.539\,\mathrm{mas\,yr^{-1}}$). But, as shown in Fig. 4.1, component C4 is only detected by the TANAMI array and was never seen by Tingay and Edwards (2002). That can be explained by an increase in sensitivity similar to the situation presented by Tingay and Edwards (2002). Their component C1 was only detected by the VLBA and not by SHEVE. They pointed out that SHEVE is less sensitive than the VLBA. Hence, the outer components (C2, C3, C4) can be neglected for the kinematic analysis, if the

whole period of nearly 20 years from 1992 November to 2012 September is considered. Figure 4.1 also shows that there are two possibilities to combine the data of Tingay and Edwards (2002) with the TANAMI data. The components C2 and C3 of Tingay and Edwards (2002) can in both cases be identified with the components C7 and C8 of the TANAMI data. But, on the one hand side, the component C1 of Tingay and Edwards (2002) can be identified with component C6 of the TANAMI data (left panel). On the other hand side, it can be split into two components identified with the two components C5 and C6 of the TANAMI data (right panel). Since it is not clear what version should be used for the calculations, the components C5 and C6 should also be neglected for the analysis. Therefore, only the components C7 and C8 are taken into account, which are the only components that are observed during the whole period. Hence, the largest possible apparent speed becomes $\beta_{\mathrm{app}} = 0.36$ for component C7 ($< 0.095\,\mathrm{mas\,yr^{-1}}$). But nevertheless, as pointed out in Sect. 3.2, the components C7 and C8 are consistent with stationary features without significant motion.

According to Tingay and Edwards (2002) it is not possible to tightly constrain the jet orientation or speed with the limits of this thesis, namely $R > 95$ (see Sect. 3.1) and $\beta_{\mathrm{app}} \leq 0.36$, as well as the limits on the Doppler factor from Ghisellini et al. (1993) ($\delta > 1$) and Dondi and Ghisellini (1995) ($\delta > 1.3$). However, these limits can be used to calculate the allowed region of the $\beta - \phi$ plane that satisfies these constraints. Therefor the Equations for the apparent speed β_{app} (Equation (1.1.11)), the Doppler factor δ (Equation (1.1.12)) and the ratio of the observed flux densities R (Equation (1.1.14)) have to be converted into Equations for the jet speed β depending on the viewing angle ϕ. Solving Equation (1.1.11) for β yields

$$\beta = \frac{\beta_{\mathrm{app}}}{\sin\phi + \beta_{\mathrm{app}}\cos\phi}\,, \tag{4.1.1}$$

solving Equation (1.1.12) for β yields

$$\beta = \frac{\delta\cos\phi \pm \sqrt{1 + \cos^2\phi - \delta^2}}{1 + \cos^2\phi} \tag{4.1.2}$$

and solving Equation (1.1.14) for β yields

$$\beta = \frac{1}{\cos\phi}\frac{R^{1/p} - 1}{R^{1/p} + 1}\,. \tag{4.1.3}$$

With these three Equations the curves shown in Fig. 4.2 and Fig. 4.3 are computed, where the red-colored ones belong to the limits obtained from this thesis and the blue-colored ones belong to the limits presented by Tingay and Edwards (2002). The exponent p in Equation (4.1.3) is chosen to be $p = 3 + \alpha$, if R is estimated using only one jet component (red and blue curves). Furthermore, also curves for the exponent $p = 2 + \alpha$, that must be taken into account, if R is calculated using the flux densities of the complete

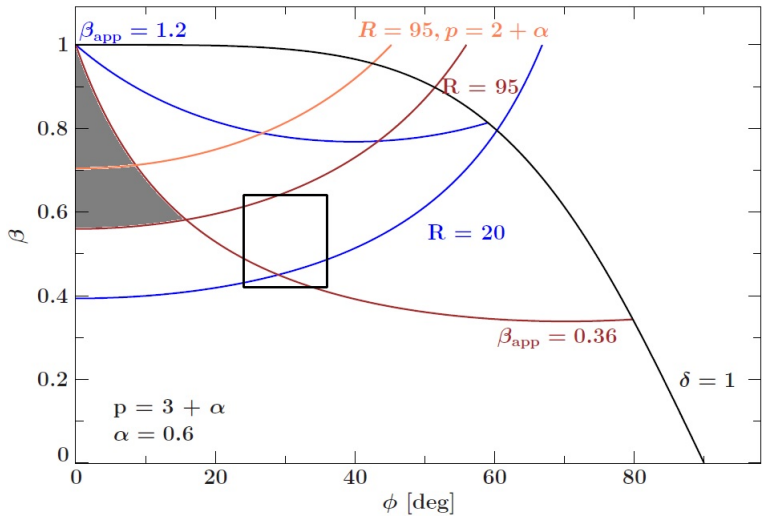

Figure 4.2.: The region of the $\beta - \phi$ plane that satisfies the constraints $\delta > 1$, $\beta_{\text{app}} < 0.36$ and $R > 95$ is shaded in gray. The region of the plane that satisfies the constraints of Tingay and Edwards (2002), namely $\delta > 1$, $\beta_{\text{app}} < 1.2$ and $R > 20$, is embedded by the two blue-colored curves. The region of the plane that satisfies the constraints of Pian et al. (1996), namely $0.42 \leq \beta \leq 0.64$ and $\phi = 30° \pm 6°$, is shown as the boxed region. This region is completely ruled out. The curve for $\delta = 1$ was computed using Equation (4.1.2), the curves for β_{app} were computed using Equation (4.1.1) and the curves for R were computed using Equation (4.1.3) with $p = 3 + \alpha$ (red and blue curve) and $\alpha = 0.6$, according to Tingay and Edwards (2002). A curve for $R = 95$ and $p = 2 + \alpha$ is also plotted in orange, showing that varying the exponent p has only little consequences on the essential results.

jet and counterjet structure, are plotted (orange-colored) for a comparison. But, as one can see, varying the exponent p has only little consequences on the essential results. For the spectral index a value of $\alpha = 0.6$, measured by Tingay and Edwards (2002) for their component C1, was chosen for the calculations.

Similar to the discussion of Tingay and Edwards (2002) Fig. 4.2 shows the region of the $\beta - \phi$ plane (shaded in gray) that satisfies the observational constraints of $R > 95$, $\beta_{\text{app}} < 0.36$ and $\delta > 1$, according to the Doppler factor estimates of Ghisellini et al. (1993). The area between the two blue-colored curves represents the allowed region of the $\beta - \phi$ plane estimated by Tingay and Edwards (2002), satisfying the constraints $R > 20$, $\beta_{\text{app}} < 1.2$ and $\delta > 1$, and the boxed area represents the results of Pian et al. (1996), namely a Lorentz factor of $\gamma = 1.2 \pm 0.1$, leading to $0.42 \leq \beta \leq 0.64$, and a jet angle to the line of sight of $\phi = 30° \pm 6°$. One can see that the region that satisfies the constraints of Tingay and Edwards (2002) is diminished to the region shaded in gray, inferring a minimal jet speed of $\beta \gtrsim 0.56$ and a maximum of the viewing angle of $\phi \lesssim 16°$. Therefore, this new area matches the viewing angle of $6° \leq \phi \leq 15°$

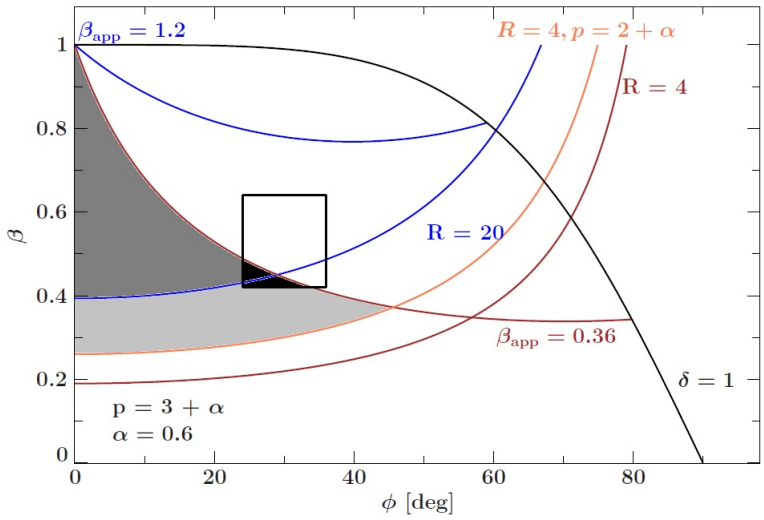

Figure 4.3.: The region of the $\beta - \phi$ plane that satisfies the constraints $\delta > 1$, $\beta_{\text{app}} < 0.36$ and $R > 4$ is shaded in gray. The region of the plane that satisfies the constraints of Tingay and Edwards (2002), namely $\delta > 1$, $\beta_{\text{app}} < 1.2$ and $R > 20$, is embedded by the two blue-colored curves. The overlap of this two regions are shaded in dark gray. The region of the plane that satisfies the constraints of Pian et al. (1996), namely $0.42 \leq \beta \leq 0.64$ and $\phi = 30° \pm 6°$, is shown as the boxed region. Only the small part shaded in black satisfies also the constraints of this thesis. But, differently to the situation shown in Fig. 4.2, this region is not completely ruled out. The curve for $\delta = 1$ was computed using Equation (4.1.2), the curves for β_{app} were computed using Equation (4.1.1) and the curves for R were computed using Equation (4.1.3) with $p = 3 + \alpha$ (red and blue curve) and $\alpha = 0.6$, according to Tingay and Edwards (2002). A curve for $R = 4$ and $p = 2 + \alpha$ is also plotted in orange, showing that varying the exponent p has only little consequences on the essential results. Here the orange curve was chosen to be the lower limit for the allowed region, because R was computed using the flux densities of the complete jet and counterjet structures.

obtained by D'Ammando et al. (2015) very well, but leads to the fact that the boxed area, corresponding to the constraints of Pian et al. (1996), is completely ruled out. This implies that the results of Pian et al. (1996) could be false. Otherwise, this results were confirmed by ALMA observations presented by Leon et al. (2016) (see Sect. 2.1).

But, as one can see in Fig. 4.2, the red-colored curve, representing the constraint $\beta_{\text{app}} < 0.36$, crosses the boxed area. So, for smaller R at least a small part of the boxed area is located in the region that satisfies the constraints of this thesis. This could be obtained if the existence of a possible counterjet was taken into account. As mentioned in Sect. 3.1 a total minimum of the ratio of the observed flux densities was computed to be $R > 4$ using a possible jet and counterjet structure. Figure 4.3 illustrates the allowed region of the $\beta - \phi$ plane, calculated using $R > 4$ (shaded in gray), where the overlap of

this region and the area that satisfies the constraints of Tingay and Edwards (2002) is shaded in dark-gray. The small part of the boxed area that lies in the allowed region is shaded in black. Here, the orange-colored curve, representing the R constraints for the exponent $p = 2 + \alpha$, is chosen as the lower limit for the allowed region, because R was computed by using the flux densities of the complete jet and counterjet structure. One can see that the allowed region of the $\beta-\phi$ plane now marginally allows for the parameter constraints of Pian et al. (1996). Given the better representation of the data with the no-counterjet model (see Sect. 3.1), it seems unlikely that the VLBI results can be reconciled with the large viewing angle constrained from multiwavelength observations discussed previously in the literature.

4.2. Flux Density and Brightness Temperature of the Core Component

Until 2010 March the flux density of the core component was computed to be $1.16\,\mathrm{Jy} \leq S_{\mathrm{core}} \leq 1.52\,\mathrm{Jy}$, implying that the flux density remains constant within the conventional uncertainties of $15-20\%$ (Ojha et al. 2010). Figure 4.4 illustrates the flux density of the core component as a function of time. One can see that there is an increase after 2010 March with a maximum value of $S_{\mathrm{max}} = 2.60\,\mathrm{Jy}$ in 2011 April. This increase of the flux density corresponds to the γ-ray flaring activity between 2010 June and 2012 February presented by D'Ammando et al. (2015) and shown in Fig. 4.5.

The brightness temperature of the core component is plotted in Fig. 4.6 as a function of time. One can see that the brightness temperature is less than the inverse Compton limit of $10^{12}\,\mathrm{K}$ (see Sec. 1.1.3) until 2010 March and in 2012 September. Only between 2010 July and 2011 November the brightness temperature exceeds the inverse Compton limit with a maximum value of $T_{\mathrm{B,\,max}} = 8.48 \cdot 10^{12}\,\mathrm{K}$ in 2011 November. This period also corresponds to the γ-ray flaring activity between 2010 June and 2012 February shown in Fig. 4.5 (D'Ammando et al. 2015). Hence, the three high brightness temperatures above the inverse Compton limit can also be explained by the γ-ray flaring activity, similar to the increase of the flux density during this period.

The brightness temperatures of the other six epochs are less than the inverse Compton limit, but only in the two epochs marked with the red triangles, where the core component is completely resolved, the brightness temperatures are computed using the estimated major and minor axes of the core component. The other temperatures are computed using the resolution limits of the major and minor axes, listed in Table 3.7, of the core component and therefore, they are only lower limits of the brightness temperature. Nevertheless, the two brightness temperatures, computed using the estimated major and minor axes of the core component, can be compared with the brightness temperature of $6^{+\mathrm{inf}}_{-5} \cdot 10^{11}\,\mathrm{K}$ computed by Tingay and Edwards (2002). Thereby, the brightness temperature of the 2009 February epoch, with a value of $3.88 \cdot 10^{11}\,\mathrm{K}$, is

somewhat less than this value and the brightness temperature of the 2012 September epoch, with a value of $8.26 \cdot 10^{11}$ K, is somewhat higher than this value. But, within the uncertainties, they are very well compatible with the value calculated by Tingay and Edwards (2002).

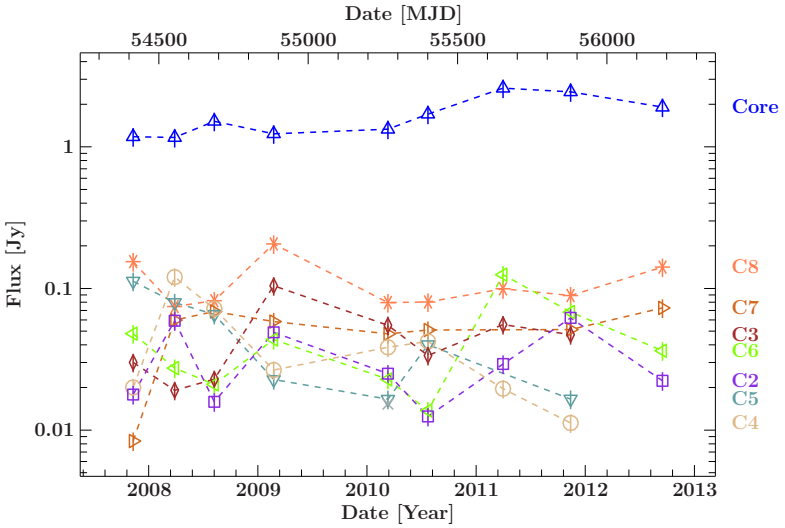

Figure 4.4.: The flux densities of the jet components are plotted as a function of time. The error bars are set to 15% of the value of the flux density. According to Ojha et al. (2010) the conventional uncertainties are given by $15 - 20\%$. Until 2010 March the flux density of the core component is constant within these uncertainties. Thereafter, one can see an increase of the flux density of the core component corresponding to the γ-ray flaring activity shown in Fig. 4.5 (D'Ammando et al. 2015).

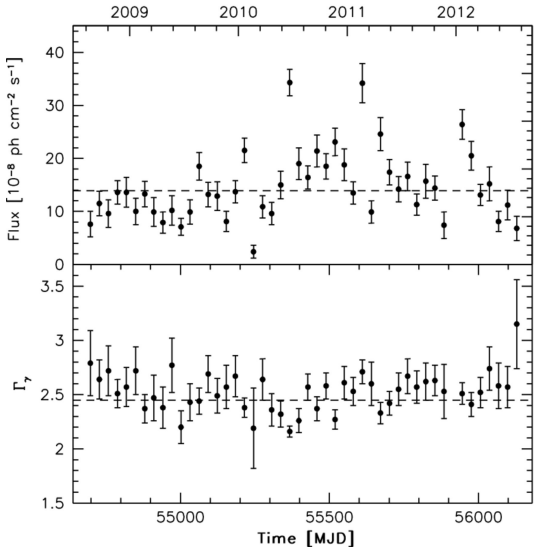

Figure 4.5.: The $0.1 - 100\,\mathrm{GeV}$ flux showing the flaring activity between 2010 June and 2012 February of PKS 0521−365 (top panel) and the photon index from a power-law model (bottom panel). The dashed line in both panels represents the mean value. Taken from D'Ammando et al. (2015).

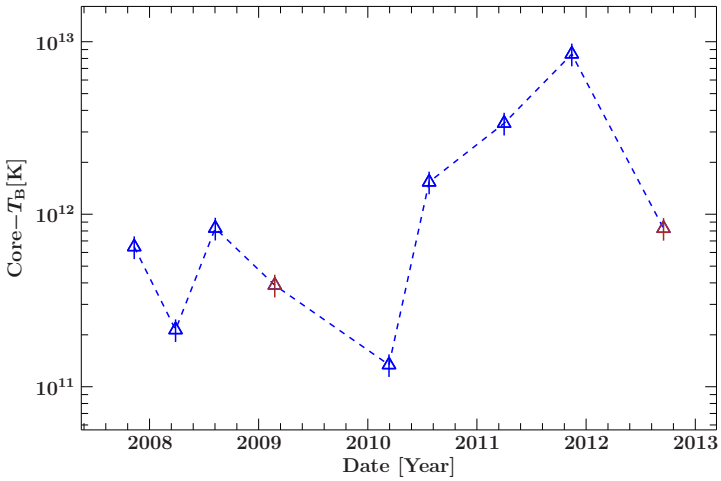

Figure 4.6.: The brightness temperature of the core component is plotted as a function of time. The error bars are set to 15% of the value of the brightness temperature, because only the flux density, with the conventional uncertainty of $15 - 20\%$ (Ojha et al. 2010), is taken into account for the error analysis. Only the two red-colored triangles mark real brightness temperatures. All other values are only lower limits, because there the core component is unresolved.

5. Conclusion and Outlook

In this thesis nine TANAMI VLBI epochs of PKS 0521−365, observed at 8.4 GHz, were investigated. The obtained images show a knotty jet structure with an extension of about 80 pc. This structure could be modeled with eight components. With this components the jet to counterjet ratio was computed to be $R > 95$. Also images with a possible counterjet were made leading to $R > 4$.

Together with VLBA and SHEVE data presented by Tingay and Edwards (2002) a kinematic analysis results in a maximum apparent speed $\beta_{\mathrm{app}} < 0.36$. For $R > 95$ this leads to a reduction of the $\beta - \phi$ plane satisfying the constraints of Tingay and Edwards (2002), namely $R > 20$, $\beta_{\mathrm{app}} < 1.2$ and $\delta > 1$. The new allowed $\beta - \phi$ plane is limited by $\beta \gtrsim 0.56$ and $\phi \lesssim 16°$ corresponding to the viewing angle presented by D'Ammando et al. (2015) lying in the range $6° \leq \phi \leq 15°$. Indeed, the area of the $\beta - \phi$ plane that satisfies the constraints of Pian et al. (1996), namely $\gamma = 1.2 \pm 0.1$, leading to $0.42 \leq \beta \leq 0.64$, and $\phi = 30° \pm 6°$, is completely ruled out. Even if $R > 4$ is used to constrain the $\beta - \phi$ plane, only a marginal fraction of the area of Pian et al. (1996) is located in the allowed $\beta - \phi$ plane. Therefore, the TANAMI VLBI data suggest a smaller inclination angle of the jet than previously thought.

The flux density of the core component is nearly constant until 2010 March. Thereafter it shows an increase corresponding to the γ-ray flaring activity between 2010 June and 2012 February (D'Ammando et al. 2015). In this period also the brightness temperature of the core component exceeds the inverse Compton limit of 10^{12} K, which can also be explained by the γ-ray flaring activity. The other temperatures are between the equipartition value of 10^{11} K and the inverse Compton limit. Because the core component is unresolved in most epochs, the computed brightness temperatures of these epochs are lower limits. Only in two epochs the core component was resolved, namely in 2009 February and 2012 September, leading to brightness temperatures of $3.88 \cdot 10^{11}$ K and $8.26 \cdot 10^{11}$ K which are very well compatible to the brightness temperature computed by Tingay and Edwards (2002) of $6^{+\mathrm{inf}}_{-5} \cdot 10^{11}$ K within the uncertainties.

PKS 0521−365 is an AGN with an unclear classification. It is classified as a BL Lac object or radio galaxy. But also with the results of this thesis a statement about this topic can not be given. Therefore, higher resolved observations at higher frequencies are needed to get more information for the classification of PKS 0521−365. Furthermore, because it is not clear whether there is a counterjet or not, VLBI observations with higher sensitivity are needed to answer this question.

A. Appendix

A.1. (u, v)-plane Coverages

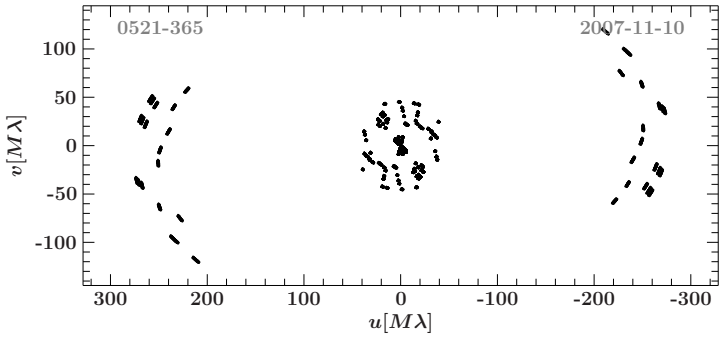

Figure A.1.: (u, v)-plane coverage of the 2007-11-10 epoch of PKS 0521−365.

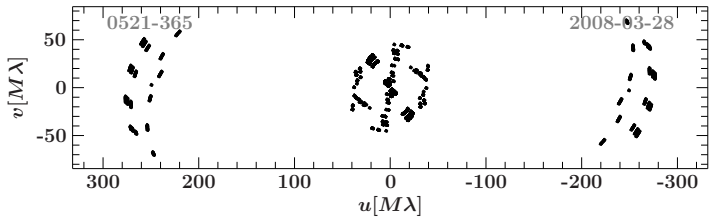

Figure A.2.: (u, v)-plane coverage of the 2008-03-28 epoch of PKS 0521−365.

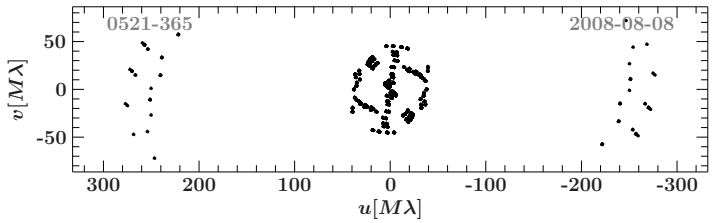

Figure A.3.: (u, v)-plane coverage of the 2008-08-08 epoch of PKS 0521−365.

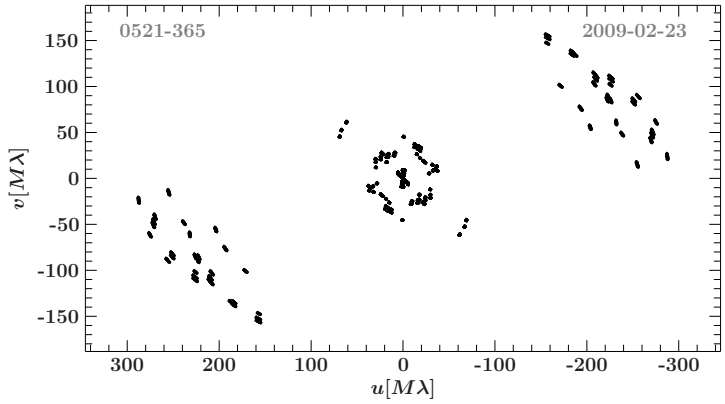

Figure A.4.: (u, v)-plane coverage of the 2009-02-23 epoch of PKS 0521−365.

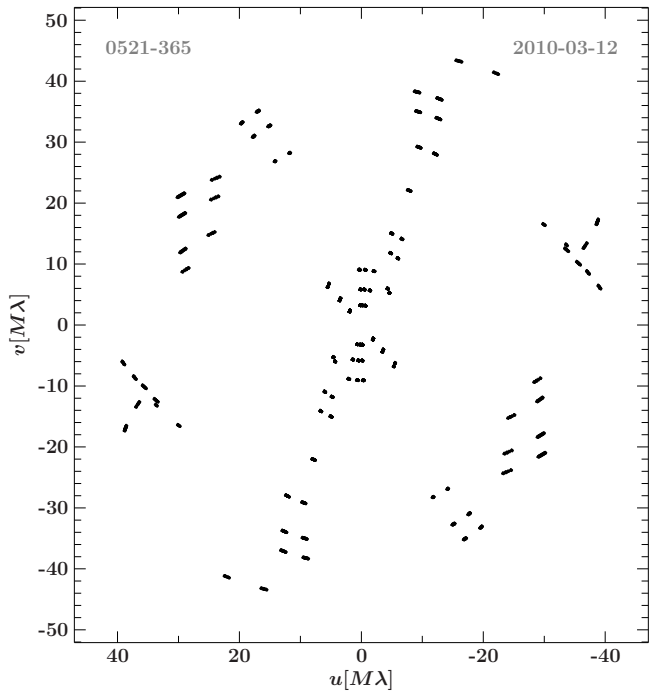

Figure A.5.: (u, v)-plane coverage of the 2010-03-12 epoch of PKS 0521−365.

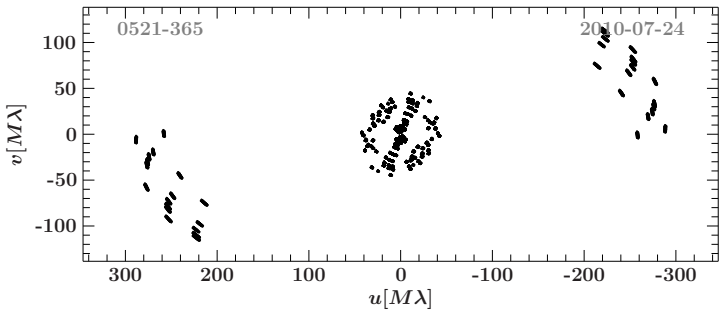

Figure A.6.: (u, v)-plane coverage of the 2010-07-24 epoch of PKS 0521−365.

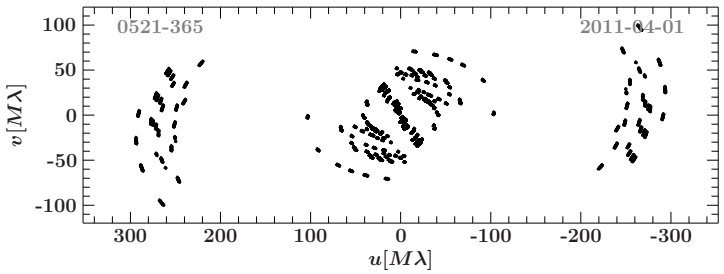

Figure A.7.: (u, v)-plane coverage of the 2011-04-01 epoch of PKS 0521−365.

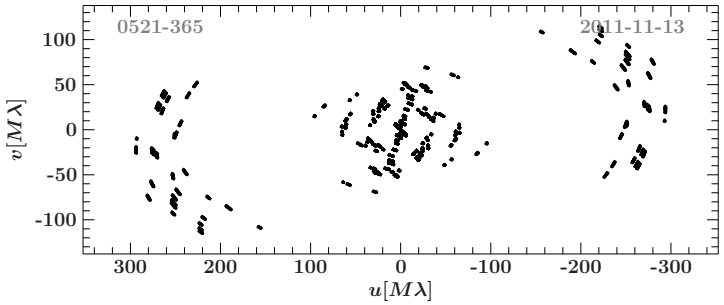

Figure A.8.: (u, v)-plane coverage of the 2011-11-13 epoch of PKS 0521−365.

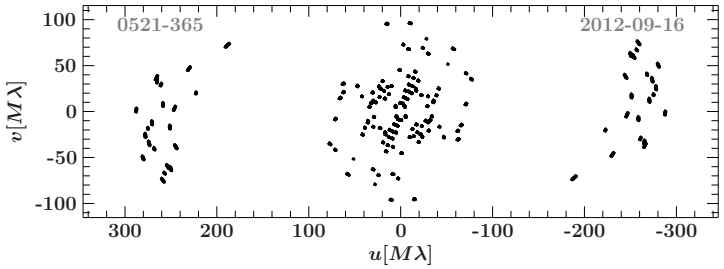

Figure A.9.: (u, v)-plane coverage of the 2012-09-16 epoch of PKS 0521−365.

A.2. Images of PKS 0521−365

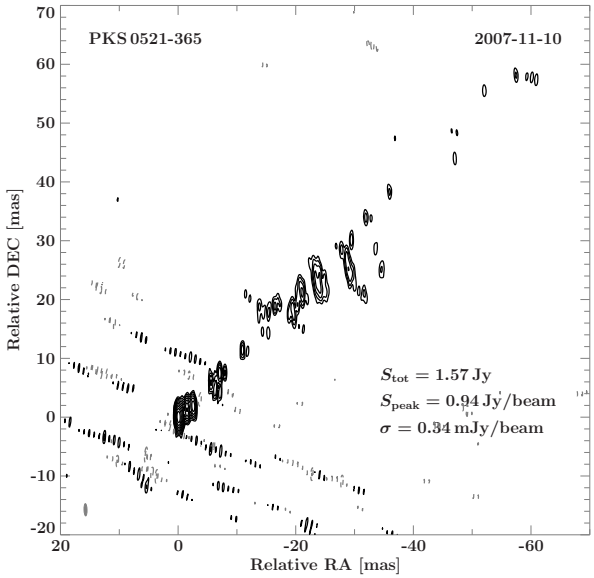

Figure A.10.: Image of PKS 0521−365 in the 2007-11-10 epoch. $S_{\rm tot}$ is the total flux density, $S_{\rm peak}$ is the peaked flux density of the core and $\sigma_{\rm rms}$ is the noise level. The gray ellipse in the bottom left corner corresponds to the beam. The contours begin at 3σ and increase logarithmically by factors of 2.

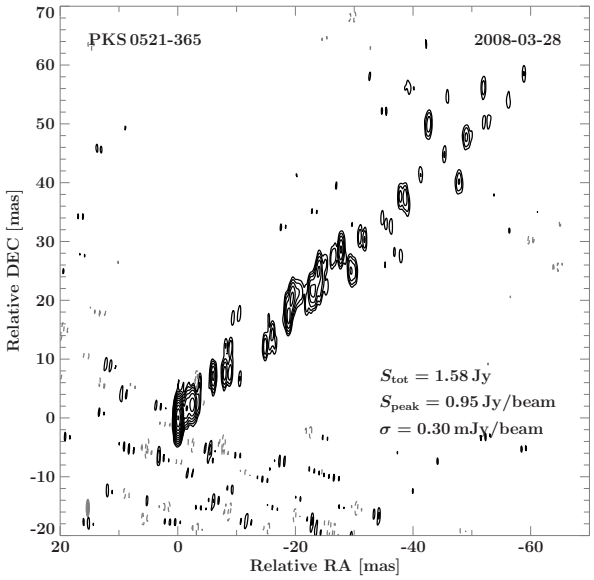

Figure A.11.: Image of PKS 0521−365 in the 2008-03-28 epoch. $S_{\rm tot}$ is the total flux density, $S_{\rm peak}$ is the peaked flux density of the core and $\sigma_{\rm rms}$ is the noise level. The gray ellipse in the bottom left corner corresponds to the beam. The contours begin at 3σ and increase logarithmically by factors of 2.

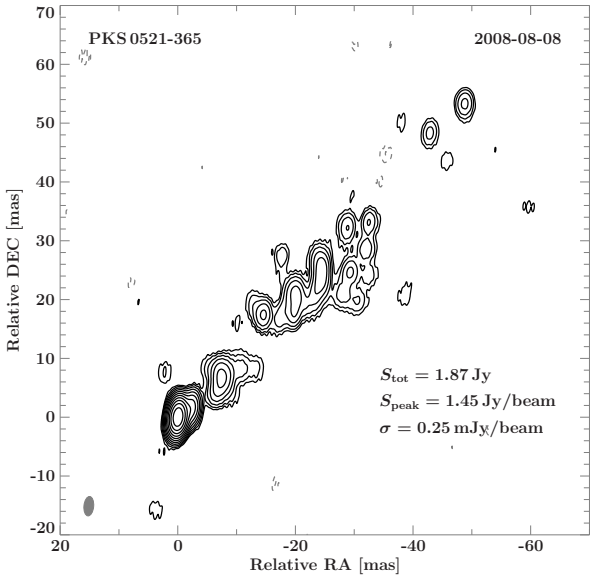

Figure A.12.: Image of PKS 0521−365 in the 2008-08-08 epoch. $S_{\rm tot}$ is the total flux density, $S_{\rm peak}$ is the peaked flux density of the core and $\sigma_{\rm rms}$ is the noise level. The gray ellipse in the bottom left corner corresponds to the beam. The contours begin at 3σ and increase logarithmically by factors of 2.

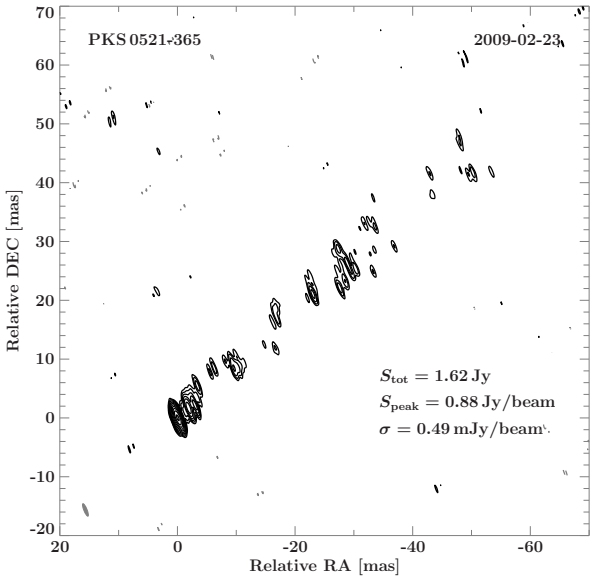

Figure A.13.: Image of PKS 0521−365 in the 2009-02-23 epoch. $S_{\rm tot}$ is the total flux density, $S_{\rm peak}$ is the peaked flux density of the core and $\sigma_{\rm rms}$ is the noise level. The gray ellipse in the bottom left corner corresponds to the beam. The contours begin at 3σ and increase logarithmically by factors of 2.

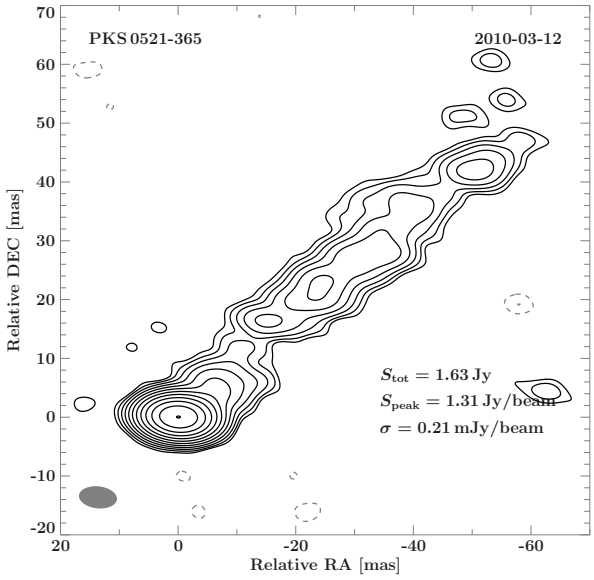

Figure A.14.: Image of PKS 0521−365 in the 2010-03-12 epoch. $S_{\rm tot}$ is the total flux density, $S_{\rm peak}$ is the peaked flux density of the core and $\sigma_{\rm rms}$ is the noise level. The gray ellipse in the bottom left corner corresponds to the beam. The contours begin at 3σ and increase logarithmically by factors of 2.

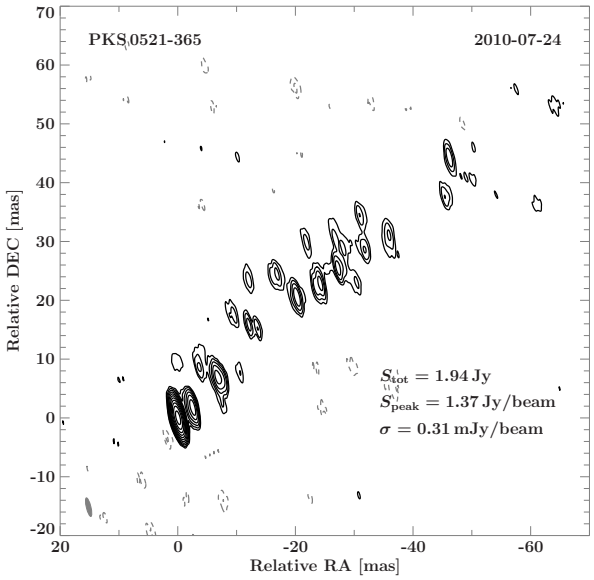

Figure A.15.: Image of PKS 0521−365 in the 2010-07-24 epoch. $S_{\rm tot}$ is the total flux density, $S_{\rm peak}$ is the peaked flux density of the core and $\sigma_{\rm rms}$ is the noise level. The gray ellipse in the bottom left corner corresponds to the beam. The contours begin at 3σ and increase logarithmically by factors of 2.

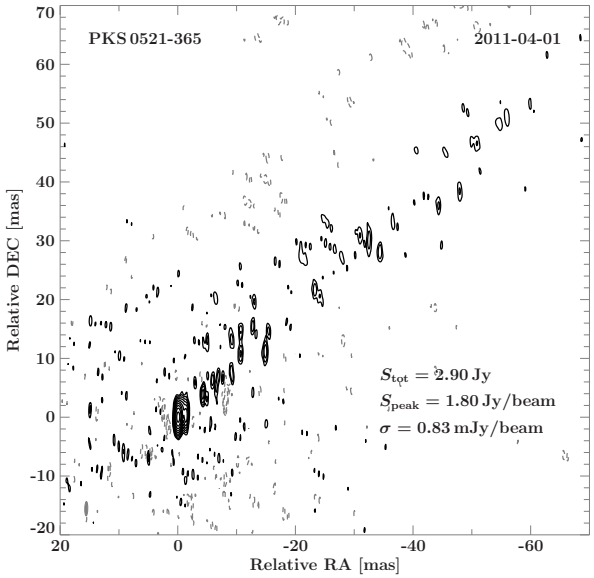

Figure A.16.: Image of PKS 0521−365 in the 2011-04-01 epoch. $S_{\rm tot}$ is the total flux density, $S_{\rm peak}$ is the peaked flux density of the core and $\sigma_{\rm rms}$ is the noise level. The gray ellipse in the bottom left corner corresponds to the beam. The contours begin at 3σ and increase logarithmically by factors of 2.

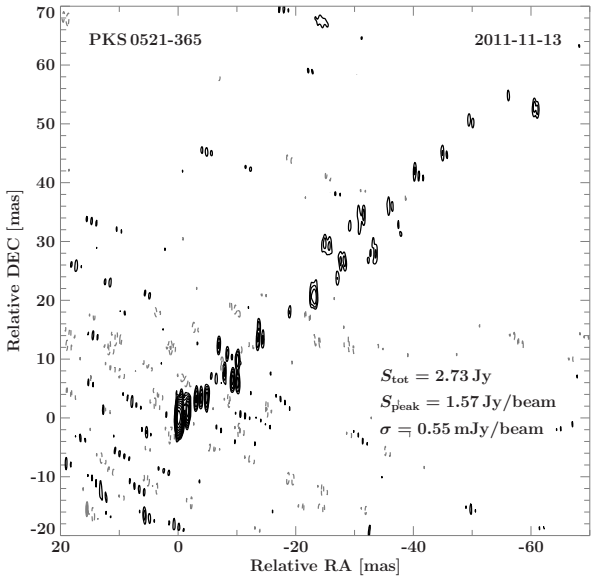

Figure A.17.: Image of PKS 0521−365 in the 2011-11-13 epoch. $S_{\rm tot}$ is the total flux density, $S_{\rm peak}$ is the peaked flux density of the core and $\sigma_{\rm rms}$ is the noise level. The gray ellipse in the bottom left corner corresponds to the beam. The contours begin at 3σ and increase logarithmically by factors of 2.

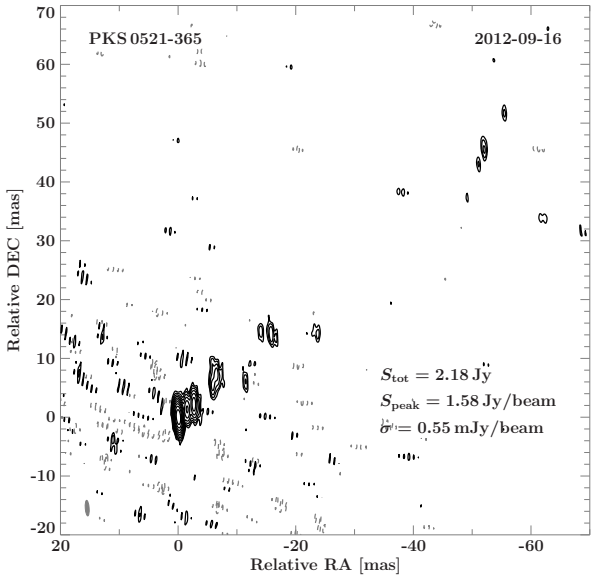

Figure A.18.: Image of PKS 0521−365 in the 2012-09-16 epoch. $S_{\rm tot}$ is the total flux density, $S_{\rm peak}$ is the peaked flux density of the core and $\sigma_{\rm rms}$ is the noise level. The gray ellipse in the bottom left corner corresponds to the beam. The contours begin at 3σ and increase logarithmically by factors of 2.

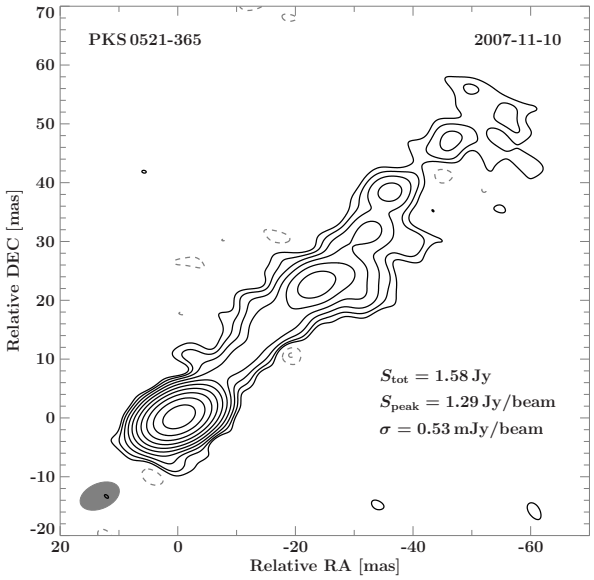

Figure A.19.: Tapered image of PKS 0521−365 in the 2007-11-10 epoch. $S_{\rm tot}$ is the total flux density, $S_{\rm peak}$ is the peaked flux density of the core and $\sigma_{\rm rms}$ is the noise level. The gray ellipse in the bottom left corner corresponds to the beam. The contours begin at 3σ and increase logarithmically by factors of 2.

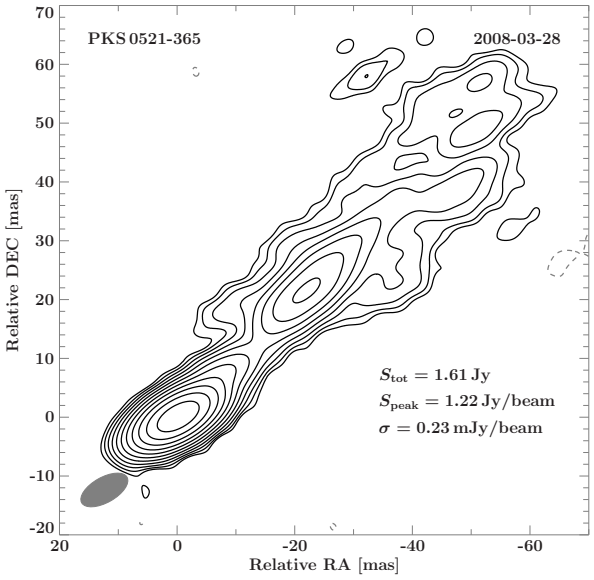

Figure A.20.: Tapered image of PKS 0521−365 in the 2008-03-28 epoch. $S_{\rm tot}$ is the total flux density, $S_{\rm peak}$ is the peaked flux density of the core and $\sigma_{\rm rms}$ is the noise level. The gray ellipse in the bottom left corner corresponds to the beam. The contours begin at 3σ and increase logarithmically by factors of 2.

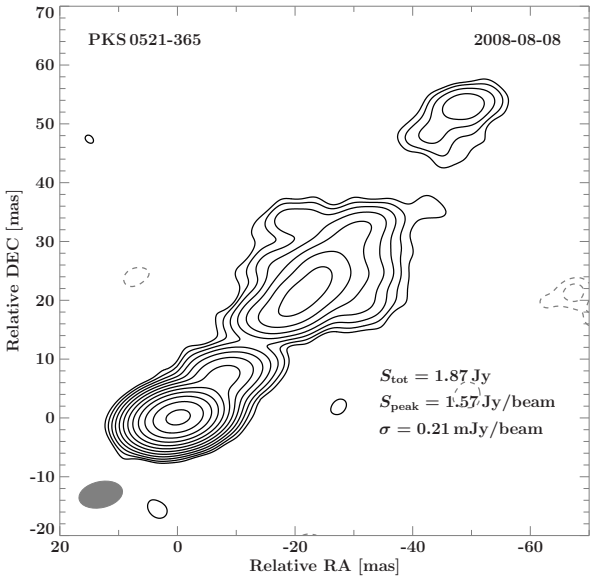

Figure A.21.: Tapered image of PKS 0521−365 in the 2008-08-08 epoch. $S_{\rm tot}$ is the total flux density, $S_{\rm peak}$ is the peaked flux density of the core and $\sigma_{\rm rms}$ is the noise level. The gray ellipse in the bottom left corner corresponds to the beam. The contours begin at 3σ and increase logarithmically by factors of 2.

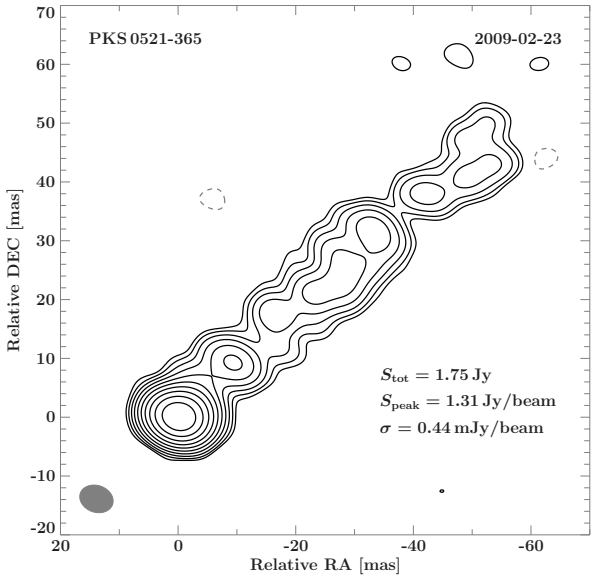

Figure A.22.: Tapered image of PKS 0521−365 in the 2009-02-23 epoch. $S_{\rm tot}$ is the total flux density, $S_{\rm peak}$ is the peaked flux density of the core and $\sigma_{\rm rms}$ is the noise level. The gray ellipse in the bottom left corner corresponds to the beam. The contours begin at 3σ and increase logarithmically by factors of 2.

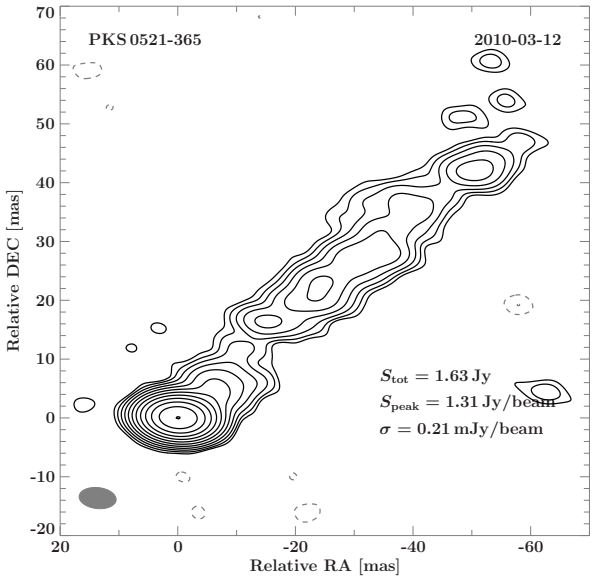

Figure A.23.: Tapered image of PKS 0521−365 in the 2010-03-12 epoch. $S_{\rm tot}$ is the total flux density, $S_{\rm peak}$ is the peaked flux density of the core and $\sigma_{\rm rms}$ is the noise level. The gray ellipse in the bottom left corner corresponds to the beam. The contours begin at 3σ and increase logarithmically by factors of 2.

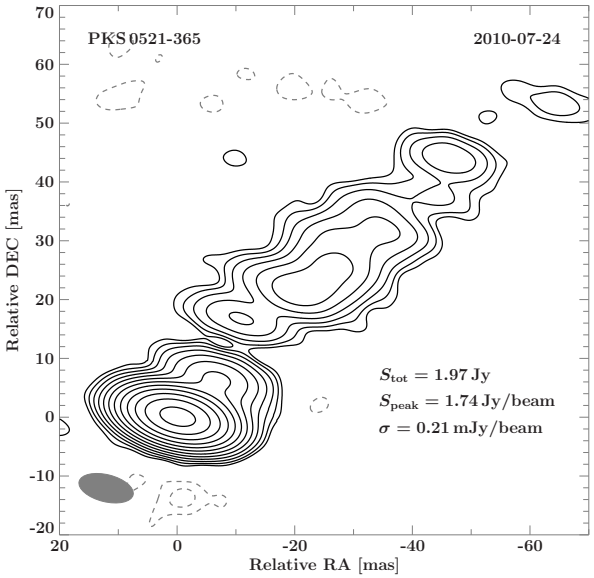

Figure A.24.: Tapered image of PKS 0521−365 in the 2010-07-24 epoch. $S_{\rm tot}$ is the total flux density, $S_{\rm peak}$ is the peaked flux density of the core and $\sigma_{\rm rms}$ is the noise level. The gray ellipse in the bottom left corner corresponds to the beam. The contours begin at 3σ and increase logarithmically by factors of 2.

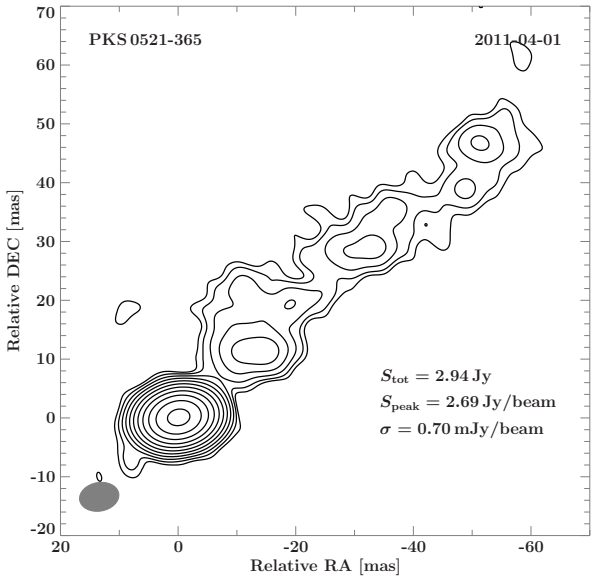

Figure A.25.: Tapered image of PKS 0521−365 in the 2011-04-01 epoch. $S_{\rm tot}$ is the total flux density, $S_{\rm peak}$ is the peaked flux density of the core and $\sigma_{\rm rms}$ is the noise level. The gray ellipse in the bottom left corner corresponds to the beam. The contours begin at 3σ and increase logarithmically by factors of 2.

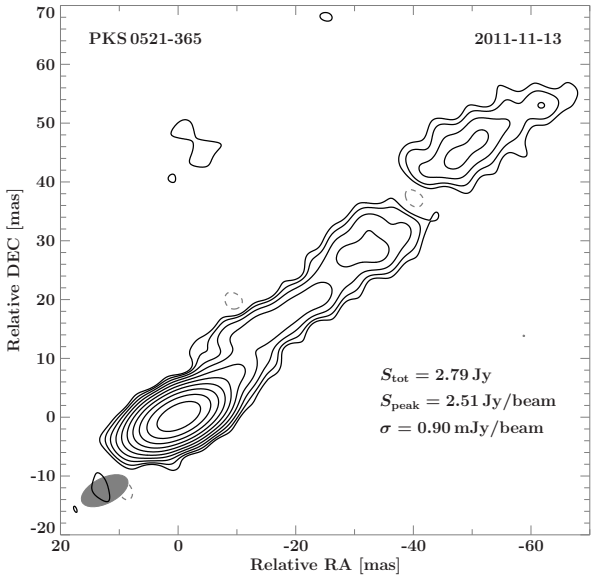

Figure A.26.: Tapered image of PKS 0521−365 in the 2011-11-13 epoch. $S_{\rm tot}$ is the total flux density, $S_{\rm peak}$ is the peaked flux density of the core and $\sigma_{\rm rms}$ is the noise level. The gray ellipse in the bottom left corner corresponds to the beam. The contours begin at 3σ and increase logarithmically by factors of 2.

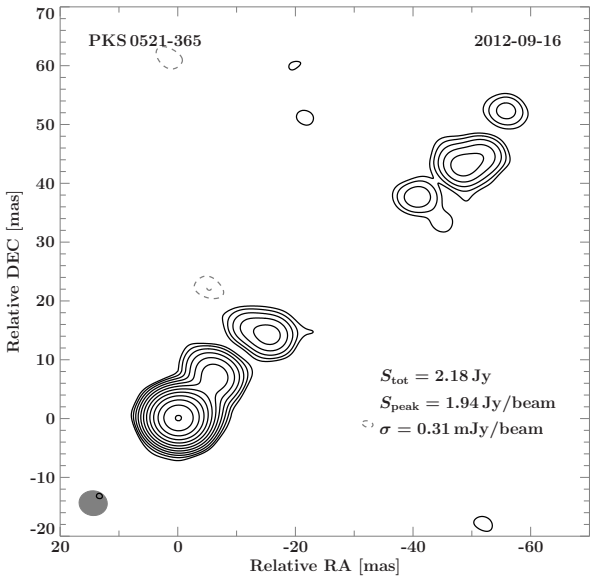

Figure A.27.: Tapered image of PKS 0521−365 in the 2012-09-16 epoch. $S_{\rm tot}$ is the total flux density, $S_{\rm peak}$ is the peaked flux density of the core and $\sigma_{\rm rms}$ is the noise level. The gray ellipse in the bottom left corner corresponds to the beam. The contours begin at 3σ and increase logarithmically by factors of 2.

Bibliography

Antonucci R., 1993, ARA&A 31, 473

Blandford R.D., Königl A., 1979, ApJ 232, 34

Böck M., 2012, PhD thesis, Naturwissenschaftliche Fakultät, Friedrich-Alexander-Universität Erlangen-Nürnberg

Böttcher M., 2010, Fermi meets Jansky - AGN at Radio and Gamma-Rays, Ed. by Savolainen T., Ros E., Porcas R. W. and Zensus J. A., Bonn

Burke B. F., Graham - Smith F., 2010, An Introduction to Radio Astronomy, Cambridge University Press

Carroll B. W., Ostlie D. A., 2014, An Introduction to Modern Astrophysics, Second Edition, Pearson Education Limited

Cotton W. D., 1995, Very Long Baseline Interferometry and the VLBA, Ed. by Zensus J. A., Diamond P. J. and Napier P. J., Vol. 82, Astronomical Society of the Pacific Conference Series

D'Ammando F., Orienti M., Tavecchio F., et al., 2015, MNRAS 450, 3975

Dondi L., Ghisellini G., 1995, MNRAS, 273, 583

Diamod P. J., 1995, Very Long Baseline Interferometry and the VLBA, Ed. by Zensus J. A., Diamond P. J. and Napier P. J., Vol. 82, Astronomical Society of the Pacific Conference Series

Falomo R., Pian E., Treves A., et al., 2009, A&A 501, 907

Fanaroff B.L., Riley J.M., 1974, MNRAS 167, 31P

Felli M., Spencer R. E., 1989, Very Long Baseline Interferometry Techniques and Applications, Kluwer Academic Publishers

Ghisellini G., Padovani P., Celotti A., Maraschi L., 1993, ApJ 407, 65

Greisen E. W., 2003, Information Handling in Astronomy - Historical Vistas, Vol. 285, p. 109, Kluwer Academic Publishers

Högbom J. A., 1974, Astron. Astrophys. Suppl. 15, 417

Houck J. C., DeNicola L. A., 2000, Astronomical Data Analysis Software and Systems IX, Ed. by Manset N., Veillet C. and Crabtree D., Vol. 216, Astronomical Society of the Pacific Conference Series

Kadler M., 2015, Extragalactic jets, Lecture on extragalactic jets held in the summer term

Kadler M., Ojha R., & TANAMI Collaboration, 2015, AN 336, 499

Kellermann K. I., Moran J. M., 2001, ARA&A 39, 457

Kellermann K. I., Pauliny-Toth I. I. K., 1969, ApJ 155, 71

Kellermann K. I., Sramek R., Schmidt M., et al., 1989, AJ 98, 1195

Kembhavi A. K., Narlikar J. V., 1999, Quasars and Active Galactic Nuclei An Introduction, Cambridge University Press

Kovalev Y. Y., Kellermann K. I., Lister M. L., et al., 2005, ApJ 130, 2473

Leon S., Cortes P. C., Guerard M., et al., 2016, A&A 586, A70

Mannheim K., 1993, A&A 269, 67

Mannheim K., Biermann P. L., 1992, A&A 253, L21

Müller C., 2014, PhD thesis, Institut für Physik und Astronomie, Julius-Maximilians-Universität Würzburg

Ojha R., Kadler M., Böck M., et al., 2010, A&A 519, 45

Pian E., Falomo R.,Ghisellini G., et al., 1996, ApJ 459, 169

Readhead A. C. S., 1994, ApJ 426, 51

Rybicki G. B., Lightman A. P., 1979, Radiativ Processes in Astrophysics, New York: Wiley

Seyfert C.K., 1943, ApJ, 97, 28

Shepherd M. C., 1997, Astronomical Data Analysis Software and Systems VI, Ed. by Hunt G. and Payne H. E., Vol. 125, Astronomical Society of the Pacific Conference Series

Tingay S. J., Edwards P. G., 2002, AJ 124, 652

Taylor G., 1997, The DIFMAP Cookbook

Urry C.M., Padovani P., 1995, PASP 107, 803

Danksagung

An dieser Stelle möchte ich mich bei all denjenigen bedanken, die zum Gelingen meiner Bachelorarbeit beigetragen haben.

Ganz besonders möchte ich mich bei meinem Betreuer Prof. Dr. Matthias Kadler dafür bedanken, dass er mir die Möglichkeit gegeben hat, dieses interessante Projekt zu bearbeiten. Durch viele aufschlussreiche Diskussionen und hilfreiche Ratschläge unterstützte er mich immer hilfsbereit bei aufkommenden Problemen.

Außerdem möchte ich mich bei Robert Schulz bedanken, vor allem für seine Unterstützung im Umgang mit ISIS. Auch er war bei vielen Diskussionen zugegen und gab mir viele hilfreiche Tipps.

Ich möchte mich auch bei Till Steinbring für das Korrekturlesen der Arbeit bedanken. Seine Hinweise halfen mir sehr dabei, die Arbeit zu verbessern.

Des weiteren möchte ich mich bei allen Mitarbeitern des Lehrstuhls für Astronomie, unter der Leitung von Prof. Dr. Karl Mannheim, und besonders bei den Mitgliedern der AG Kadler, für die herzliche Aufnahme und Unterstützung bedanken.

Auch bei meinen Kommilitonen aus dem Bachelor Büro, Michael Blank, Manuel Dörr, Amar Hekalo, Johannes Kammerer, Stefan Lindeholz und Juliane Wiehl, möchte ich mich für die angenehme Arbeitsatmosphäre und die vielen hilfreichen Diskussionen bedanken.

Zum Schluss möchte ich mich noch bei meinen Eltern bedanken, die mich während meines ganzen Studiums unterstützt haben und immer für mich da sind.

Selbstständigkeitserklärung

Hiermit erkläre ich, dass die vorliegende Arbeit nach allgemeiner Studien- und Prüfungsordnung für die Bachelor- und Masterstudiengänge (ASPO) an der Julius-Maximilians-Universität Würzburg selbstständig und nur unter Benutzung der angegebenen Quellen und Hilfsmittel angefertigt wurde. Des weiteren wurde die Arbeit noch keiner anderen Prüfungsbehörde zur Erlangung eines akademischen Grades vorgelegt.

Würzburg, 21. April 2016 Florian Rösch